Ultrafast pulse propagation in graphene-comprising nanophotonic waveguides considering non-perturbative electrodynamic nonlinearity

ALEXANDROS PITILAKIS[1,*] AND EMMANOUIL E. KRIEZIS[1]

[1]*School of Electrical and Computer Engineering, Aristotle University of Thessaloniki, Thessaloniki 541 24, Greece*
[*]*Corresponding author: alexpiti@auth.gr*

We outline a comprehensive model for ultrafast optical pulse propagation along nonlinear graphene-comprising integrated photonic waveguides. An electrodynamic graphene hot-electron model (GHEM) is used to capture the temporal dynamics and intertwined absorptive and refractive nonlinearity to explore a strongly non-perturbative photoconductivity regime that transcends third-order phenomena. We propose a formalism to abstract the 2D material-related modal properties of the waveguides in the static/continuous wave regime that can also be plugged into a generalized nonlinear Schrödinger equation (NLSE) framework. Our model of optical pulse propagation consists of a coupled NLSE along with the nonlinear equation system of the GHEM. We demonstrate pulsed applications pertinent to integrated photonic components, namely: improvement of the extinction ratio of a non-return-to-zero (NRZ) modulated bitstream, pulse shaping, spectral broadening, and optical-shock formation leading to pulse breaking and soliton formation. Our NLSE-GHEM extracts graphene nonlinearity from fundamental physics without resorting to phenomenological correction terms or fitted parameters, shows good agreement with recent experiments, and can potentially be used in the study of high-power on-chip applications such as pulsed lasers and frequency combs.

1. INTRODUCTION

The last decade has witnessed a steady increase in high-power applications of integrated graphene-comprising waveguides [1], since the first evidence of its large third-order NIR nonlinearity [2]. Graphene, the most extensively studied 2D material [3], has multiple attributes that are attractive to photonic integrated circuits (PIC), its most important being the electrical tunability of its optical conductivity [4] and the compatibility to the silicon platform [5]. The combination of these two properties has thus far given a large number of low-power/linear regime applications in passive and tunable graphene-comprising PICs, such as modulators [6–8], switches [9–11], and photodetectors [12, 13]. In contrast, the high-power/nonlinear applications in PICs have mostly been limited to proofs-of-concept and attempts to accurately quantify graphene nonlinearity (GNL) [14–18]. It must be pointed out that light-matter interaction in PICs is quantitatively different than in nonlinear structures typically studied by focused laser and THz beams, i.e., normal incidence on graphene sheets lying on dielectric substrates [19, 20] or sandwiched between fibers [21].

One of the reasons behind the slow pacing in high-power/nonlinear applications in graphene-comprising PICs is the emerging understanding of the intricacies in GNL and, arguably, the starting point: GNL was initially approached as a third-order process, similar to that arising in bulk nonlinear semiconductor such as silicon [22]. Early theoretical studies based on semi-classical and full-quantum mechanic approaches [23–25] produced a wide spectrum of values for graphene's third-order surface conductivity tensor, $\sigma^{(3)}$, which was then used in photonic and hybrid-plasmonic waveguide engineering [26, 27]. While experimental evidence in free-space structures partially corroborated the theoretical trends and unveiled interesting aspects pertaining to the refractive part sign of the nonlinearity [28, 29], the dependence of the GNL magnitude on the 2D material properties, e.g., the sample's equivalent chemical potential (Fermi energy) and quality (carrier mobility, level of impurities), remained unclear. Moreover, experiments with nanophotonic waveguides accessed a GNL regime that was phenomenologically richer, containing both refractive and absorptive contribu-

tions, and more strongly nonlinear, in a manner that could not be modeled in a classical perturbative third-order framework [14, 17, 18]. These results hint that an electrodynamic model is more suitable [16, 30], as it properly treats the hot free-carrier plasma that is photogenerated in graphene when illuminated by high optical intensities, quite similar to the effects in bulk/3D semiconductors [31].

The work presented in this paper takes this last avenue, i.e., it consolidates refractive and absorptive non-perturbative GNL in a single *graphene hot-electron model* (GHEM) [32] and further adapts it to ultrafast pulse propagation along highly-confining nanophotonic waveguides, by means of the generalized nonlinear Schrödinger equation (NLSE) framework. Our approach replaces the disjoint phenomenological treatments of GNL {e.g., quasi-perturbative third-order nonlinearity [16], saturable absorption (SA) [18, 33, 34], and saturable photo-excited carrier refraction (SPCR) [17]} with a single comprehensive model, which can be used to model and interpret a large class of nonlinear phenomena in graphene-comprising waveguides. The GHEM seamlessly incorporates all parameters related to graphene's electro-optical tunability, fabrication quality, and associated temporal dynamics [35–37]. We formally extract eigenmode-specific parameters for the NLSE in a formalism that is applicable to any waveguide (fiber or integrated) and any nonlinear 2D material [38, 39]. Finally, to showcase the potential of this NLSE-GHEM approach, we present examples of pulsed applications in emerging nanophotonic waveguide platforms [40], that can be extended to on-chip pulsed laser platforms [41] or frequency combs [42], where cavity build-up produces intensity levels that necessitate the usage of a GHEM.

The remainder of this paper is organized as follows: Section 2 outlines the NLSE framework and the extraction of its parameters from rigorous waveguide analysis. Section 3 describes the GHEM used to produce the photoconductivity (nonlinearity) of graphene. Section 4 deals with the optimization of the waveguide and the graphene monolayer in static conditions and validates the NLSE parameters extracted. Section 5 presents ultrafast pulsed-regime examples computed with the NLSE-GHEM and showcases a number of applications and emerging nonlinear phenomena. Section 6 concludes and summarizes the paper.

2. MODELING PULSE PROPAGATION IN NONLINEAR WAVEGUIDES

A. Nonlinear Schrödinger Equation Framework

One of the most popular methods for modeling pulse propagation along nonlinear optical waveguides is the NLSE framework [43]. It relies on the slowly-varying envelope approximation (SVEA) allowing only the temporal envelope of a signal to be propagated in a reflectionless manner along a nonlinear waveguide. Even though the NLSE is strictly valid close to a central/carrier frequency, it can accurately treat wideband and ultrafast signals as long as the dispersive properties of the waveguide are rigorously treated [44].

The NLSE was first used for low-nonlinearity bulk structures such as optical fibers [43] and then expanded to nanophotonic diffraction-limited and/or higher-nonlinearity structures such as integrated semiconductor waveguides [22]. The standard form of the NLSE treats dispersion together with perturbative refractive third order nonlinear phenomena such as the Kerr effect (self-phase modulation), cross-phase modulation (in dual-channel), or generalized four-wave mixing (for three or more
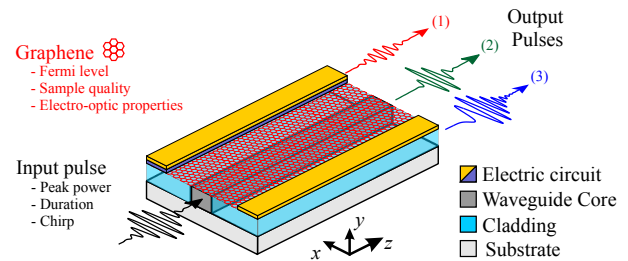

Fig. 1. Schematic of the pulse propagation along an integrated graphene-comprising nonlinear waveguide. The distortion of the output pulse can range between cases such as: (1) linear absorption, (2) temporal compression, or (3) frequency chirping, depending on input pulse and graphene properties. For tuning the latter, an abstracted electric circuit is also depicted.

channels). Absorption, linear and perturbative/third-order, can easily be introduced in the NLSE, while more complicated nonlinearities, absorptive or refractive, need more careful treatment. For instance, free-carrier absorption (FCA) and dispersion (FCD, also called plasma refraction) in silicon and hybrid photonic waveguides [22, 45, 46] requires heuristically introduced correction terms that couple the NLSE to other rate-equations that need to be solved in parallel.

The advent of 2D materials, with electrically-tunable graphene at its forefront, brought new aspects to the NLSE formalism. Electromagnetically, graphene can be formally modeled by surface conductivities $\sigma^{(m)}$ in units of $[S(m/V)^{(m-1)}]$, with $m = 1$ and 3 corresponding to linear and third-order nonlinear (perturbative) conductivities, respectively. The introduction of graphene to nonlinear integrated waveguides started with the rigorous re-definition of third-order nonlinear parameters based on its surface conductivity tensor [26, 27, 47] and moved on to modeling the more advanced nonlinear effects in graphene, such as SA [33, 34, 48] or SPCR [17, 30]. Despite some theoretical works [23–25], most of these formulations relied on specific experimental measurement or phenomenological estimation of macroscopic graphene properties, e.g., its third order surface conductivity $\sigma^{(3)}$ [29, 49], equivalent nonlinear index $n_{2,eq}$ [27, 50], or saturation intensity I_{sat} [33]. Therein lies the gap that our work aims to bridge: We adopt a microscopic electrodynamic GHEM for the complex (absorptive and refractive) nonlinearity of graphene which we adapt to the NLSE, effectively allowing for proper treatment of non-perturbative nonlinearity induced by ultrawideband signals such as the ones produced by pulsed sub-ps lasers. Moreover, the GHEM inherently introduces the tunability of graphene through its chemical potential μ_0, a value that can be tailored at fabrication or electrically reconfigured by gating [16] or biasing [6]. An abstracted schematic of the structure studied in this work is depicted in Fig. 1, where the graphene and waveguide properties can be used to calculate the output pulse distortion from the nonlinear waveguide.

The photoconductivity $\Delta\sigma^{(1)}_{NL} = \sigma^{(1)}_{NL} - \sigma^{(1)}_{lin}$ [where $\sigma^{(1)}_{lin}$ is the linear conductivity of graphene in the absence of irradiation or, more generally, in a low-power regime], i.e., the light-induced change in its surface conductivity, is modeled as a free-carrier effect using the GHEM and is then plugged as an extra time-dependent term in the NLSE, $\delta_{GNL}(z, t)$, similar to how FCD/FCA are treated in silicon and hybrid-plasmonic waveguides [22, 45]. The difference, here, is that $\delta_{GNL}(z, t)$ depends on the spatiotemporal pulse amplitude in a much more complicated

manner compared to the Soref model for free-carriers in silicon [31]. In this work, following the electromagnetic derivation of [34], we formulate a basic single-channel NLSE for the complex optical pulse envelope $A(z,t)$ (in units of $[W^{1/2}]$) modulating a carrier frequency ω, under the $e^{-i\omega t}$ phase convention, as

$$\frac{\partial A}{\partial z} = \left[-\frac{\alpha}{2} + B + i\gamma_{\text{NL}}|A(z,t)|^2 - \delta_{\text{GNL}}(z,t) \right] A(z,t). \quad \textbf{(1)}$$

In this compact form, the waveguide-related constants are: α is the power loss coefficient (real positive) which includes a contribution from graphene through $\text{Re}\{\sigma_{\text{lin}}^{(1)}\}$. γ_{NL} is the complex third-order nonlinear parameter (including Kerr effect and perturbatively induced nonlinear absorption or transparency which comes *exclusively* from bulk/3D nonlinear materials and is totally unrelated to graphene. Note that graphene's nonlinear response can be adequately described as a third-order phenomenon, and thus by a Kerr-type surface conductivity $\sigma^{(3)}$ and a nonlinear parameter γ_{NL}^G [26], only up to moderate illumination powers which fall short of the regime targeted in this work; nevertheless, the GHEM can be used to compute the value of this complex quasi-perturbative $\sigma^{(3)}$ [16]. B is the linear dispersion operator, including group-velocity dispersion (β_2) and higher,

$$B = \sum_{m=2}^{\infty} i^{m+1} \frac{\beta_m}{m!} \frac{\partial^m}{\partial t^m}, \quad \textbf{(2)}$$

and t is the retarded-envelope time frame, moving with the mode group velocity. Finally, the complex-valued (z,t)-dependent term δ_{GNL}, qualitatively proportional to $\Delta\sigma_{\text{NL}}^{(1)}$, includes all nonlinear refractive and absorptive contributions from graphene. Notice how δ_{GNL} is added with a minus in Eq. (1), so that an absorption saturation characterized by $\text{Re}\{\Delta\sigma_{\text{NL}}^{(1)}\} < 0$ introduces a "gain" that counteracts the linear loss factor α. In the same sense, and recalling that self-focusing refraction corresponds to $\text{Re}\{\gamma_{\text{NL}}\} > 0$, the $\pm$ sign in $\text{Im}\{\Delta\sigma^{(1)}\}$ corresponds to a defocusing ($+$) or self-focusing ($-$) refraction.

The split-step Fourier method (SSFM) [43] is the tool used to numerically integrate the NLSE. The SSFM splits the waveguide in a cascade of segments and slides the temporal envelope of the pulse through each segment until the end of the waveguide is reached. At each of these steps it calculates the distortion due to the combined effect of the linear (α and B) and nonlinear (γ_{NL} and δ_{GNL}) terms and, of course, the pulse envelope at the input of the segment. The nonlinear (time-domain) step in Eq. (1) can be written as

$$A(z+\Delta z,t) = A(z,t)\exp\left\{\left[i\gamma_{\text{NL}}|A(z,t)|^2 - \delta_{\text{GNL}}(z,t)\right]\Delta z\right\}, \quad \textbf{(3)}$$

where Δz is the length of the waveguide segment, chosen so that the magnitude of the exponent is sufficiently small, e.g, $\pi/100$. The effect of the linear terms in Eq. (1) (absorption α and dispersion B) is more easily added in the spectral domain, where the Fourier transform is used. The SSFM algorithm iterates the time/frequency-domain operations while stepping along the z-axis until the end of the waveguide has been reached.

B. NLSE Parameters

A key assumption for the validity of the NLSE framework is that the eigenmode profile (the eigenvector) is not significantly affected by nonlinearity-induced changes in the electromagnetic properties of the materials. This assumption is valid for graphene-comprising integrated waveguides in the NIR up to a very high power threshold [48], since light guidance is provided by the underlying silicon waveguide/structure while graphene, though it interacts with the mode, does not itself guide; an obvious requirement is that the geometric waveguide dimensions and operating frequency are far from the mode cut-off.

Under this assumption, the parameters of the NLSE in Eq. (1) are extracted from spectral-domain finite-element method (FEM) modeling of the waveguide cross-section using the full-vector and/or tensor properties of the involved bulk and sheet materials [26]; note that, in the absence of magnetic biasing, graphene is an isotropic 2D material so that its $\tilde{\sigma}^{(1)}$ second-rank tensor has two nonzero elements both equal to a complex scalar value. The FEM allows for treatment of arbitrarily-shaped geometries with adjustable spatial resolution; these aspects are critical for contemporary nanophotonic waveguides with narrow features. The eigenvalue and eigenvector of the desired mode(s) of the waveguide are extracted at the specified operation frequency using a custom/in-house FEM-based mode solver [51]. The eigenvalue is typically the complex-valued effective refractive index, n_{eff}, whose imaginary part is directly related to the attenuation constant $\alpha = 2\text{Im}\{n_{\text{eff}}\}k_0$ (waveguide propagation losses) while a spectral sweep and differentiation on the real part produces the dispersion coefficients β_m of Eq. (2). The eigenvector is essentially the vector E-field profile in the cross section, $\tilde{\mathbf{e}}(\omega; x, y)$, whose post-processing yields the third-order nonlinear parameters, e.g., γ_{NL}, from bulk- or sheet-material nonlinear properties [26].

It is worth noting that for NIR optical waveguides, where graphene acts as a perturbation to the propagation mainly affecting the losses, the power attenuation coefficient of the waveguide can be calculated perturbatively, i.e., from the xy-profile of the eigenvector $\tilde{\mathbf{e}}$ of the waveguide in the absence of graphene and the graphene conductivity $\sigma^{(1)}$ as

$$\alpha = \frac{1}{2\mathcal{P}_n} \int_G \text{Re}\{\sigma^{(1)}(\omega; x, y)\}|\tilde{\mathbf{e}}_\parallel(\omega; x, y)|^2 \mathrm{d}\ell. \quad \textbf{(4)}$$

In this expression, the complex vector $\tilde{\mathbf{e}}_\parallel(\omega; x, y)$ is the E-field component of the eigenmode that is parallel to graphene at frequency ω, $\int_G \mathrm{d}\ell$ denotes integration along the trace of any graphene sheet(s) in the waveguide cross-section (xy plane)[e.g., along the thick red lines in the top-row panels of Fig. 2], and

$$\mathcal{P}_n = \frac{1}{2}\text{Re}\left\{ \iint_S (\tilde{\mathbf{e}} \times \tilde{\mathbf{h}}^*) \cdot \hat{z} \mathrm{d}x\mathrm{d}y \right\} \quad \textbf{(5)}$$

is the eigenmode's power normalization constant (subscript "n"), measured in Watt. The surface integral in Eq. (5) is in the cross section of the waveguide, i.e., in the xy plane. If graphene is spatially uniform, as is common to assume in photonic waveguides, then $\sigma^{(1)}(\omega; x, y) \to \sigma^{(1)}(\omega)$ and can thus be moved outside the integrand of Eq. (4).

Based on this observation, the $\delta_{\text{GNL}}(z,t)$ in the NLSE Eq. (1) is *proportional* to the induced photoconductivity predicted by the GHEM, $\Delta\sigma_{\text{NL}}^{(1)}(z,t) = \sigma_{\text{NL}}^{(1)}(z,t) - \sigma_{\text{lin}}^{(1)}$, as in

$$\delta_{\text{GNL}}(z,t) = \varsigma_{\text{NLSE}}\Delta\sigma_{\text{NL}}^{(1)}(z,t)/\sigma_0. \quad \textbf{(6)}$$

The proportionality factor in Eq. (6) is a real positive constant, characteristic of the specific waveguide mode, given by

$$\varsigma_{\text{NLSE}} = \frac{\sigma_0}{4\mathcal{P}_n} \int_G |\tilde{\mathbf{e}}_\parallel(\omega; x, y)|^2 \mathrm{d}\ell, \quad \textbf{(7)}$$

in [1/m] units, where graphene's universal optical conductivity $\sigma_0 = q^2/4\hbar \approx 61 \; \mu S$ (q is the electron charge and $\hbar$ is the reduced Plank constant) has replaced the conductivity inside the integrand in Eq. (4). Evidently, for a waveguide comprising a spatially uniform graphene sheet of conductivity σ_{const}, the modal power attenuation constant would be $\alpha \approx 2\varsigma_{NLSE}[\text{Re}\{\sigma_{const}\}/\sigma_0]$.

The modal parameter ς_{NLSE} of Eq. (7) translates the GHEM-predicted effective photoconductivity in graphene, $\Delta\sigma_{NL}^{(1)}(z,t)$, to nonlinear refraction and absorption in the NLSE. In order for this $\Delta\sigma_{NL}^{(1)}(z,t)$ to capture the spatial overlap of the eigenmode profile with the graphene sheet(s), inside the waveguide cross-section, an effective value for the E-field intensity must be adopted. We define an effective area for the mode-graphene overlap as

$$A_{eff}^G = 2Z_0 \mathcal{P}_n \frac{\int_G |\tilde{\mathbf{e}}_{\parallel}(\omega;x,y)|^2 d\ell}{\int_G |\tilde{\mathbf{e}}_{\parallel}(\omega;x,y)|^4 d\ell}, \qquad (8)$$

in units of [m²]. The derivation for this expression can be found in Section 1 of the Supplemental Document, and it is based on the proportionality of GNL magnitude on $|E_{\parallel}|^2$. Using this effective area, the profile-averaged (effective) intensity that feeds the GHEM to produce the $\Delta\sigma_{NL}^{(1)}$ is given by the simple formula

$$I_{eff}(z,t) = \frac{P(z,t)}{A_{eff}^G}, \qquad (9)$$

where $P(z,t) = |A(z,t)|^2$ (in Watt) is the power carried by the envelope at a (z,t) point in space and time.

To wrap-up the NLSE/SSFM procedure at a given z-segment of the waveguide with sufficiently small length Δz_i:

(i) The pulse envelope power at the start of the segment, $P(z_i,t) = |A(z_i,t)|^2$, and the segment length, Δz_i, are known.

(ii) The effective intensity, $I_{eff}(z_i,t)$, to be fed to the GHEM is calculated from Eq. (9).

(iii) Using a nonlinear model, such as the GHEM of [32] presented in Section 3, fed with the effective intensity $I_{eff}(z_i,t)$ together with graphene-dependent parameters, the effective photoconductivity $\Delta\sigma_{NL}^{(1)}(z_i,t)$ is calculated. This is, in essence, the material response as the pulse is slid (translated) along this z-segment using an ODE time-integration method; refer to the Supplemental Document, Section 6, for more details.

(iv) The photoconductivity $\Delta\sigma_{NL}^{(1)}(z_i,t)$ produces the nonlinearity-distorted pulse at the end of the z-segment, i.e., $A(z_i + \Delta z_i,t)$, using Eq. (3).

(v) Steps (ii)-(iv) can be iterated a couple of times, using the pulse power at the midpoint, $P(z_i + \Delta z_i/2,t)$, in Eq. (9) until the pulse at the end of the z-step converges.

(vi) The final pulse at the end of the step is transformed in the frequency domain for the application of the linear NLSE terms. This effect can also be split, applying "half" of it before and after the nonlinear (time-domain) step.

The NLSE/SSFM then moves on to the following z-segment of the waveguide. Finally, note that the waveguide segment length Δz_i can be adjusted along the propagation, in order to keep the exponent sufficiently small, e.g., $\varsigma_{NLSE}|\Delta\sigma_{NL}^{(1)}/\sigma_0|\Delta z_i \leq \pi/100$.
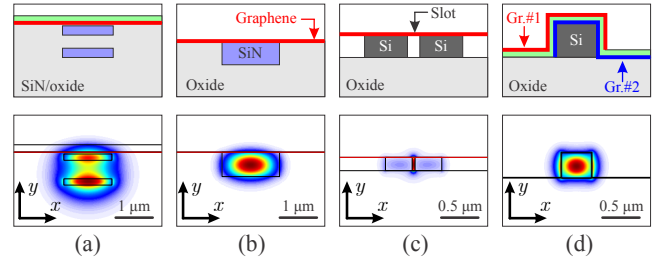

Fig. 2. A selection of graphene-comprising integrated photonic waveguides; the cross-sections and quasi-TE (x-polarized) modal intensity profiles $|\tilde{\mathbf{E}}(x,y)|^2$ are given in the top and bottom panels of each column, respectively. Graphene sheets are marked with thick red lines on top-row panels. (a) Vertical slot in SNOI [17]. (b) Buried SNOI ridge [18]. (c) Horizontal Si-slot [34, 40]. (d) Si-wire clad with two graphene sheets, marked with different colors on top panel [6].

Ref.	Type	A_{eff}^G (μm^2)	ς_{NLSE} (1/mm)
[17]	Vertical SNOI slot	4.8	3.6
[18]	Buried SNOI ridge	6.1	2.5
[34]	Horizontal SOI slot	0.05	26
[6]	Dual-graphene SOI rib	0.7	34

Table 1. Graphene nonlinearity-related parameters for the selection of integrated photonic waveguides depicted in Fig. 2.

Figure 2 presents the calculated mode profiles for a selection of integrated photonic waveguides relying on the SOI (silicon-on-insulator) and SNOI (silicon nitride-on-insulator) platforms, where graphene monolayers are marked with thick red lines. In panel (a), a vertical SNOI slot from [17], including a PMMA cladding over graphene and a few-nm oxide residual between graphene and the top SiN ridge. In panel (b), a buried SiN ridge from [18]. In panel (c), a Si-slot waveguide from [34], formed by two Si-wires spaced by a 40 nm air slot; a similar fabricated Si-slot is found in [40]. In panel (d), a Si-wire clad with two graphene sheets spaced by a thin alumina layer from [6]; when a voltage difference is applied to the two sheets, different-polarity charges are accumulated on each of the two sheets thus changing their chemical potential.

The corresponding NLSE parameters for the waveguides in Fig. 2 , i.e., the effective area A_{eff}^G from Eq. (8) and the proportionality factor ς_{NLSE} from Eq. (7), are listed in Table 1. Owing to the waveguide concept exploited, as well as the higher index contrast, the slot waveguide relying on the SOI platform offers more than a tenfold improvement in the parameters compared to the other waveguides, which means that the nonlinear power thresholds are expected to be correspondingly smaller.

Finally, we stress again that all NLSE parameters are extracted *perturbatively* here, i.e., assuming that graphene has a negligible contribution to the transverse waveguide mode profile, in the linear *and* nonlinear regimes. Moreover, the formulas developed in this section can be used for waveguide geometries with arbitrary spatial inhomogeneity in their 2D (and bulk/3D) materials.

3. A MODEL FOR GRAPHENE NIR NONLINEARITY

In the NIR, graphene's optical surface conductivity, linear and nonlinear, is primarily governed by the interband absorption mechanism which is only available when its equilibrium chemical potential is lower than the half-photon energy, $|\mu_0| < \hbar\omega/2$, owing to the Pauli exclusion principle. Above that value graphene becomes practically transparent, while for $|\mu_0| \to 0$ it exhibits the universal optical conductivity $\sigma_0 \approx 61\ \mu S$; this characteristic value is related to the 2.3% absorption by an air-suspended monolayer, as absorption in this case equals $\sigma_0 Z_0$, which moreover equals π times the fine-structure constant, $1/137$.

A. Microscopic Fermi-Dirac framework

This work relies on the electrodynamic optical nonlinearity predicted by the graphene hot-electron model (GHEM) developed in [32], which tracks several microscopic physical quantities of graphene in a Fermi-Dirac framework to finally extract the non-linear conductivity from the well established Kubo formulas. The core idea of the model is that the intraband and interband conductivities are treated separately, each one linked to a different rate equation: The intraband absorption term is responsible for heating the 2D carrier plasma, increasing its total energy density $\mathcal{E}_T^D$ (in [J/m^2]) and electronic temperature T, while the interband absorption term is responsible for photogeneration of free carriers, increasing their density by n_{PG} (in [1/m^2]); note that as electroneutrality holds, the number of photogenerated hole and electron densities is the same, equal to n_{PG}. Both absorption processes are assumed to act instantaneously (in the 10 fs timescale), but the quantities $\mathcal{E}_T^D$ and n_{PG} decay with different lifetimes; in this work we assume values in the order of $\tau_{\mathcal{E}} = 1$ ps and $\tau_{\text{rec}} = 10$ ps for the plasma energy and carrier recombination lifetimes, respectively.

A secondary aspect of the model in [32] is that a quasi-equilibrium (QE) is assumed to be instated *after* the intraband heating cools down but *before* the photogenerated carriers recombine. In this transitional QE state, the carriers have re-assumed the lattice temperature (T_0, typically 300 K) but their density and energy is still elevated. The duration of the excitation pulse as compared to the lifetimes $\tau_{\mathcal{E}}$ and τ_{rec} defines the temporal dynamics of the system: The CW analysis in [32] reveals that the magnitude of the GNL depends only on the ratio of $\tau_{\text{rec}}/\tau_{\mathcal{E}}$. Here, we consider pulse duration that falls in either of three regimes, i.e., shorter than $\tau_{\mathcal{E}} = 1$ ps (but longer than the intraband momentum relaxation lifetime, which is in the tens of fs), longer than $\tau_{\text{rec}} = 10$ ps, or in between the two.

The final aspect of the model is that it introduces separate quasi-Fermi levels (or chemical potentials) for the electron and hole plasmas in the conduction and valence band, respectively: These are $\{\mu_e, \mu_h\}$ and $\{\mu_{e_0}, \mu_{h_0}\}$ for the hot and the QE states, respectively. The relations between these quasi-Fermi levels and the carrier and plasma-energy densities can be found in Section II.B-D of [32] and are also repeated in Section 2 of the Supplemental Document of this work, for completeness.

To summarize, the model is described by the following set of six equations. The first two are the rate equations for intra- and interband mechanisms,

$$\frac{\partial \mathcal{E}_T^D}{\partial t} = \langle I_{\text{abs}} \rangle_i - \frac{\mathcal{E}_T^D - \mathcal{E}_{\text{QE}}^D}{\tau_{\mathcal{E}}}, \tag{10}$$

$$\frac{\partial n_{\text{PG}}}{\partial t} = \frac{\langle I_{\text{abs}} \rangle_e}{\hbar\omega} - \frac{n_{\text{PG}}}{\tau_{\text{rec}}} \left(1 + \frac{n_{\text{PG}}}{n_{T_0}} \right), \tag{11}$$

where $\langle I_{\text{abs}} \rangle_{i/e}$ is the effective absorbed intensity (in [W/m^2]) corresponding to the intra/interband part of graphene's conductivity and n_{T_0} is the total equilibrium (at the absence of irradiation) carrier density, mainly depending on the chemical potential μ_0. The final four equation of the model are algebraic, stemming from electroneutrality across the electron and hole carrier densities, in the hot and QE states:

$$\mu_e = +(k_B T) F_1^{-1} \left[\frac{\pi(\hbar v_F)^2}{2(k_B T)^2} (n_e^0 + n_{\text{PG}}) \right], \tag{12a}$$

$$\mu_h = -(k_B T) F_1^{-1} \left[\frac{\pi(\hbar v_F)^2}{2(k_B T)^2} (n_h^0 + n_{\text{PG}}) \right], \tag{12b}$$

$$\mu_{e_0} = +(k_B T_0) F_1^{-1} \left[\frac{\pi(\hbar v_F)^2}{2(k_B T_0)^2} (n_e^0 + n_{\text{PG}}) \right], \tag{12c}$$

$$\mu_{h_0} = -(k_B T_0) F_1^{-1} \left[\frac{\pi(\hbar v_F)^2}{2(k_B T_0)^2} (n_h^0 + n_{\text{PG}}) \right]. \tag{12d}$$

In these formulas, k_B is the Boltzmann constant, $v_F \approx c_0/300$ (c_0 is the speed of light in vacuum) is the Fermi velocity of carriers in graphene, F_1^{-1} is the inverse of the Fermi-Dirac integral of first order [see Eq. (S11) in the Supplemental Document], and $n_{e/h}^0$ are the electron/hole carrier densities at equilibrium.

The transient/pulsed-excitation solution of the six-equation system of the GHEM [Eqs. (10-11) and (12a-d)] is done using an ODE time-integration method, as discussed in Section A. The static/CW solution, i.e., when the LHS of Eqs. (10-11) is zero, involves a nonlinear equation-system solver. Refer to the Supplemental Document, Section 6, for implementation details.

B. Calculating the Nonlinear Surface Conductivity

In order to compute the nonlinear surface conductivity of graphene, we feed the GHEM with a static CW or a pulsed excitation introduced through the $\langle I_{\text{abs}} \rangle_{i/e}$ terms in Eqs. (10)/(11), respectively. In the ideal case of a uniform plane-like wave propagating along a flat monolayer in the z-axis, the effective absorbed intensity is simply

$$\langle I_{\text{abs}} \rangle_{i/e}(z,t) = \frac{1}{2} \text{Re}\{\sigma_{i/e}^{(1)}(z,t)\} |\mathbf{E}_\parallel(z,t)|^2, \tag{13}$$

where $|\mathbf{E}_\parallel(z,t)|$ is the magnitude of the E-field component parallel to the graphene sheet, in that particular point in space and time (z,t). In the case of a waveguide structure, one must account for the overlap of the modal field profile (now a 2D function in the cross section of the waveguide, xy plane) with any graphene sheets [16, 34]. This spatial overlap can be quantified in the effective value for the E-field intensity in Eq. (9), i.e., $|E|_{\text{eff}}^2 = 2Z_0 I_{\text{eff}}$, resulting in

$$\langle I_{\text{abs}} \rangle_{i/e}(z,t) = Z_0 \text{Re}\{\sigma_{i/e}^{(1)}(z,t)\} \frac{P(z,t)}{A_{\text{eff}}^G}, \tag{14}$$

where $P(z,t)$ is the instantaneous power of the signal's slowly varying envelope at point-z along the waveguide. Note that the model in [32] treats a zero-dimensional structure, i.e., a focused laser beam impinging normally on a graphene sheet, so that $\langle I_{\text{abs}} \rangle_{i/e}$ is given by the Tinkham formula [52] which also accounts for the dielectrics above/below the sheet.

With this excitation, the equation system can be solved for its six underlying microscopic graphene quantities: $\{\mathcal{E}_T^D, n_{\text{PG}}, \mu_e, \mu_h, \mu_{e_0}, \mu_{h_0}\}$, which can be static or time-dependent, for CW or pulsed excitation, respectively. Note that the electronic temperature of graphene carriers, T, can be

considered as a dependent/implicit variable of the equation system; it is computed from the Fermi-Dirac framework formulas (refer to Supplemental Document, Section 2) that relate it to the independent variables, i.e., the quasi-Fermi levels and the plasma energy/carrier densities. Finally, the triplet $\{T, \mu_e, \mu_h\}$, fully describing the microscopic properties of graphene in the hot state, together with the operating frequency ω, can be passed to the Kubo formulas for the calculation of the complex intraband and interband conductivity terms, as follows:

$$\sigma_i^{(1)}(\omega, \mu_e, \mu_h, T) = \sigma_0 \frac{i}{\pi k_B T} \int_0^\infty \frac{\mathcal{E}}{\hbar\omega + i\Gamma_i(\mathcal{E})}$$
$$\times \left[\cosh^{-2}\left(\frac{\mathcal{E} - \mu_e}{2k_B T}\right) + \cosh^{-2}\left(\frac{\mathcal{E} + \mu_h}{2k_B T}\right) \right] d\mathcal{E}, \quad \textbf{(15)}$$

and

$$\sigma_e^{(1)}(\omega, \mu_e, \mu_h, T) = \sigma_0 \frac{4i}{\pi} \int_0^\infty \frac{\hbar\omega + i\Gamma_e(\mathcal{E})}{[\hbar\omega + i\Gamma_e(\mathcal{E})]^2 - 4\mathcal{E}^2}$$
$$\times \left[\frac{1}{1 + \exp\left(\frac{-\mathcal{E} - \mu_h}{k_B T}\right)} - \frac{1}{1 + \exp\left(\frac{\mathcal{E} - \mu_e}{k_B T}\right)} \right] d\mathcal{E}, \quad \textbf{(16)}$$

respectively, where $\Gamma_{i/e}$ are the momentum scattering rates for the intra/interband processes. In this model it is assumed that the conductivity follows the parameters $\{T, \mu_e, \mu_h\}$, which can be time dependent with fluctuations down to the 100 fs scale as momentum relaxation lifetimes are typically in the order of 10 fs.

In this generalized form of the Kubo equations, we have assumed arbitrary energy-dependence in $\Gamma_{i/e} = \Gamma_{i/e}(\mathcal{E})$. Now, in practice, while the interband rate is constant and negligibly small (e.g., $\Gamma_e = 0.5$ meV), the energy-dependence and the magnitude of the intraband rate is nontrivial and crucial for the nonlinear response. Γ_i can be directly related to the quality of the graphene sample and, specifically, to the density of charged impurities, which, is in turn related to the sample's carrier mobility. In the following parts of this work we have adopted the fitting for $\Gamma_i(\mathcal{E})$ proposed in Eq. (19) of [32] with parameters $\zeta = 4$ and $\mathcal{E}_{\text{imp}} = 30$ meV. Now, the intraband conductivity can be calculated by the energy-integral in Eq. (15), which can be cast in simpler forms [26] for constant Γ_i and/or equilibrium states where $\mu_e \equiv \mu_h = \mu_0$. Note that the interband term cannot be calculated directly by Eq. (16) due to a singularity in its integrand at half-photon energy, $\mathcal{E} = \hbar\omega/2$; this can fortunately be circumvented by a transformation involving a principal value integral [53] as outlined in Section 3 of the Supplemental Document.

The final graphene photoconductivity, i.e., the irradiation-induced change in its complex-valued surface conductivity with respect to the equilibrium (low-power, linear) value, is given by:

$$\Delta\sigma_{\text{NL}}^{(1)} = \sigma_{\text{tot}}^{(1)}(\omega, \mu_e, \mu_h, T) - \sigma_{\text{tot}}^{(1)}(\omega, \mu_0, \mu_0, T_0), \quad \textbf{(17)}$$

where $\sigma_{\text{tot}}^{(1)} = \sigma_i^{(1)} + \sigma_e^{(1)}$ from Eq. (15) and Eq. (16). Note that at high-power illumination, $T > T_0$ and $\mu_e \neq \mu_h \neq \mu_0$.

C. Indicative GHEM response

Concluding the presentation of the GHEM, we evaluate the total nonlinear photoconductivity of graphene in the ideal case of a plane-like wave of given intensity propagating along an infinite flat monolayer. In this case, the photoconductivity that will be calculated refers to a specific z-position along the sheet, where the plane wave has the aforementioned intensity value and its
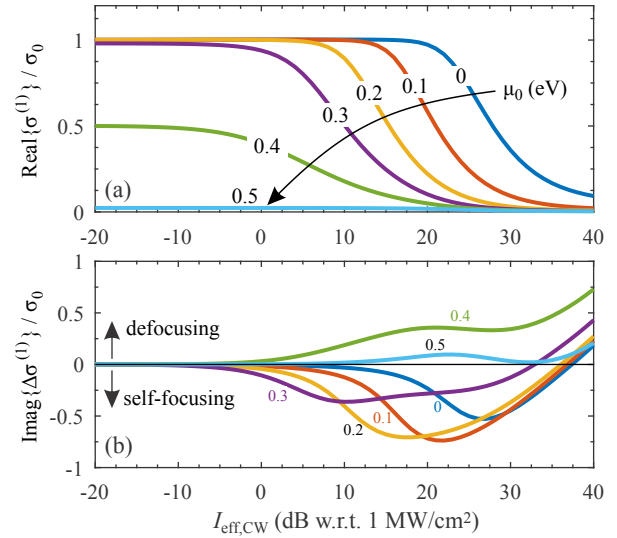

Fig. 3. Static nonlinear surface conductivity predicted by the GHEM as a function of incident intensity for a few equilibrium chemical potential values. (a) Real part, (b) shift in imaginary part, both normalized to σ_0.

polarization is parallel to the sheet; naturally, the photoconductivity magnitude is attenuated as the wave propagates along the sheet as part of it is absorbed.

In the results depicted in Fig. 3 and 4, for CW and pulsed excitation, respectively, we have assumed $\lambda_0 = 1550$ nm and $T_0 = 300$ K along with the values for $\tau_{\mathcal{E}}$, τ_{rec} and $\Gamma_{i/e}$ mentioned in the previous Sections. In both figures, different-color curves correspond to different equilibrium chemical potentials of a graphene monolayer (μ_0), assumed in a range of values that can be typically attained by electrostatic biasing [6] or gating [16]. Note that the sign of μ_0 is irrelevant for the nonlinearity in this GHEM, i.e., the exact same $\Delta\sigma_{\text{NL}}^{(1)}$ values are predicted for $\pm\mu_0$, owing to the symmetry of the charge carriers in graphene near the point of the Dirac cone.

Starting from the real part of the static/CW nonlinear conductivity, Fig. 3(a), we immediately notice the SA phenomenon: When the intensity exceeds a threshold value, the real part drops almost to zero, approximately following the phenomenologically anticipated $1/(1 + \rho)$ trend [21]. The value of the saturation intensity, I_{sat}, depends on μ_0 and decreases as $\mu_0 \to \hbar\omega/2$; however, at half-photon energy and above the real-part vanishes entirely. The refractive nonlinearity, Fig. 3(b), is captured by the shift in $\text{Im}\{\sigma^{(1)}\}$ (compared to its linear/low-power illumination value), which is found to be self-focusing for $\mu_0 < \hbar\omega/2$, defocusing close to $\hbar\omega/2$, and vanishing above that value. Exponentially increasing defocusing values are predicted for very high intensities, exceeding 10 GW/cm² (+40 dB in the horizontal axis of the graphs).

The transient response for a Gaussian pulse of 1 ps full-width half-maximum (FWHM) and 1 GW/cm² peak intensity is parametrically studied, for a few values of μ_0, in Fig. 4. The main results can be intuitively extracted from the CW response: In panel (a) we note the deep SA for $\mu_0 = 0.2$-0.4 eV, while in panel (b) we note the self/de-focusing trends. The important conclusion stemming from this transient analysis is that the exponential decay of the nonlinear conductivity to its equilibrium value happens in the τ_{rec} time span, i.e., correlates mostly with
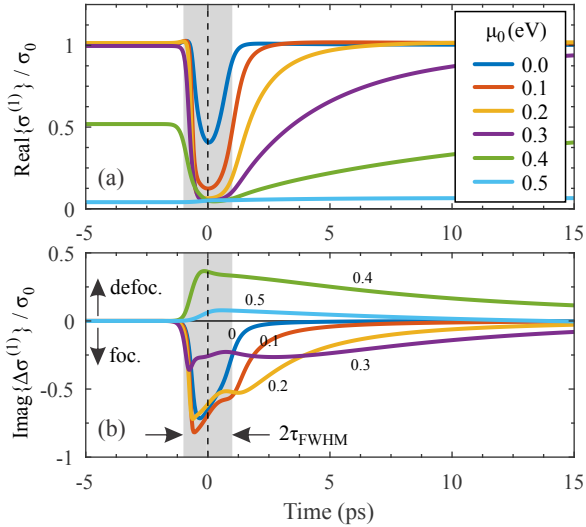
Fig. 4. Transient nonlinear surface conductivity predicted by the GHEM for a few equilibrium chemical potential values. (a) Real part, (b) shift in imaginary part, both normalized to σ_0. The grey-shaded regions correspond to twice the FWHM of the excitation pulse.

Fig. 5. Mapping the effect of the input CW intensity and equilibrium chemical potential on graphene photoconductivity. (a) SA depends only on the real part of nonlinear conductivity. (b) Refractive nonlinearity, focusing or defocusing, emerges for high $Im\{\Delta\sigma^{(1)}\}$ combined with low $Re\{\sigma^{(1)}\}$.

the photogenerated carrier density (interband absorption mechanism), as found in [17], rather than the carrier plasma heating (intraband absorption mechanism); the latter mostly contributes to small fluctuations of the imaginary part near the pulse peak.

4. STATIC/CW RESPONSE

A. Graphene Waveguide Optimization

Starting from waveguide optimization, it can be easily inferred that the optimization of the 2D-material nonlinear parameters of the NLSE (minimal A_{eff}^G and maximal ς_{NLSE}) coincides with the maximization of the linear attenuation coefficient, Eq. (4), which ensures maximal mode-graphene overlap. The comparison of the field-profiles in Fig. 2 and the extracted values in Table 1 highlights the Si-slot waveguide as the best waveguide archetype: This is due to the high index-contrast offered by the Si/air interface and the spatial overlap of graphene with the horizontally-polarized (quasi-TE) mode supported when the slot is sufficiently narrow. As waveguide optimization is not the central goal of this work, we adopt the parameters used in [34], i.e., Si-rails of 180 nm×360 nm (thickness×width) each, spaced by a 40 nm air-slot, on a silica substrate, covered by a graphene monolayer. Further optimization of this archetype can be accomplished by adding more (uncoupled) graphene layers or reducing the air-slot width and tweaking the Si-rail dimensions, as performed in Fig. 4 of [48]; nevertheless we refrain from selecting multiple graphene sheets or exaggerated dimensions, to stay close to realistic devices [40]. Note that in many fabricated devices the graphene sheets are not in contact with other semiconductors (e.g. bulk ones like silicon ridges, or other graphene sheets), but it is separated by a few-nm thickness insulating dielectric, e.g., SiO_2 in [17] or Al_2O_3 in [6]. This is because materials in physical contact with graphene affect its electrodynamic properties [32] and must be carefully accounted for. Finally, we stress that TE (horizontal) mode polarization is generally preferable to TM (vertical) in terms of light-matter interaction in integrated waveguides where the nonlinear 2D ma-
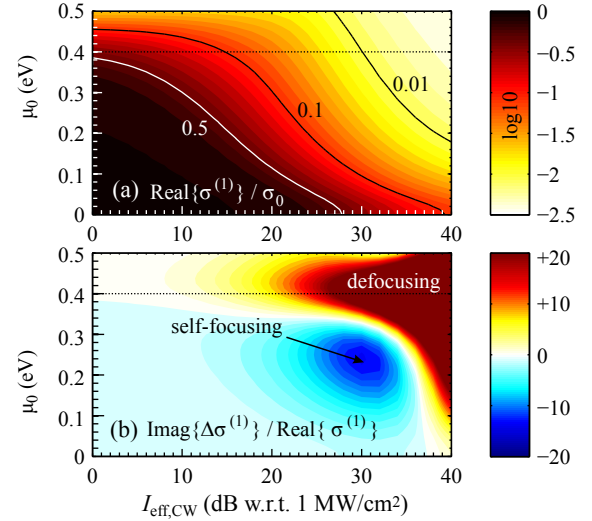
terial is very simply incorporated, i.e., as an infinite plane sheet (in the horizontal plane, xz with reference to Fig. 1) overlaying the underlying structure. TM polarization can alternatively be used, together with TE or instead of it, but this requires for engineering of the waveguide and/or potentially more complicated graphene-deposition technology; for example the 'graphene wrapped' Si-rib of Fig. 2(d) [6] exhibits low A_{eff}^G and high ς_{NLSE} for *both* TE and TM modes.

Moving on to the optimization of the graphene parameters, we mainly focus on the optimal choice of equilibrium chemical potential (μ_0) with respect to the peak-power of the illumination. The CW saturation-curves in Fig. 3 are helpful in this regard, but here we extend the parametric analysis targeted to either absorptive or refractive nonlinear functionalities. As SA is the dominant absorptive nonlinearity one aims for minimal saturation intensity I_{sat} and/or highest contrast (difference) between the losses at a low (reference) and a high intensity. These regions can be evaluated by the normalized $Re\{\sigma^{(1)}\}$ in Fig. 5(a): I_{sat} decreases as $\mu_0 \rightarrow \hbar\omega/2 = 0.4$ eV for 1550 nm operation, even down to 1 MW/cm^2, while the loss-contrast is somewhat lower in the $\mu_0 = 0.1$-0.2 eV range. Now, for optimizing refractive nonlinearity from graphene, one aims at a high $|Im\{\Delta\sigma^{(1)}\}|$ together with a low $Re\{\sigma^{(1)}\}$. These regions are identified in Fig. 5(b), where different colors are used for focusing and de-focusing refraction: There appears to be an optimal focusing-refraction combination near 0.24 eV and 1 GW/cm^2, while a defocusing region is accessible near half-photon energy (0.4 eV) and at very high powers, exceeding 10 GW/cm^2. The sign of $Im\{\Delta\sigma^{(1)}\}$ should be compared to the sign of group-velocity dispersion parameter β_2 (normal or anomalous regime), as it is key to some nonlinear phenomena like bright/dark soliton formation [43].

B. Nonlinear Self-Consistent Method

In order to validate the effective linear approximation of Eq. (6) [between the NLSE term δ_{GNL} and the GHEM photoconductivity $\Delta\sigma_{NL}^{(1)}$] and Eq. (9) [between the envelope power and the I_{eff} fed
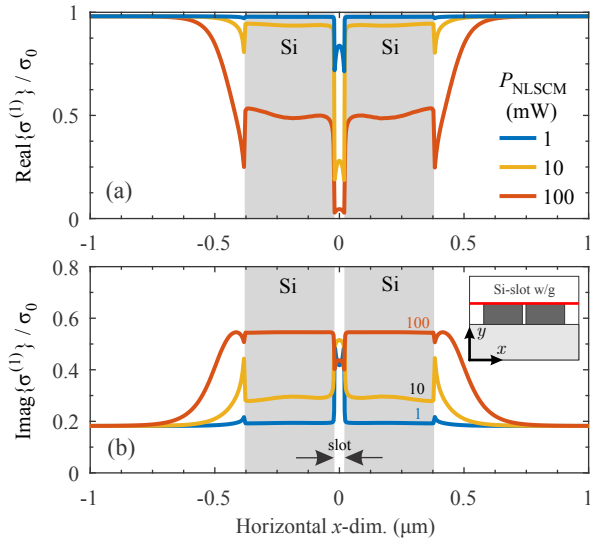
Fig. 6. NLSCM-computed spatial distribution of the nonlinear complex surface conductivity of $\mu_0 = 0.3$ eV graphene along the width of a Si-slot waveguide for a few CW power levels launched in the quasi-TE mode. (a) Real and (b) imaginary part of $\sigma^{(1)}/\sigma_0$. The grey-shaded regions correspond to the Si-rails, leaving a 40 nm air-slot between them.
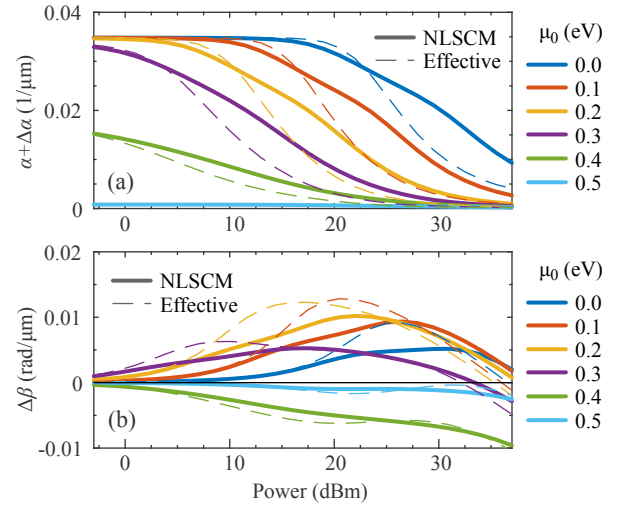

Fig. 7. Comparison between the NLSCM-calculated (thick solid curves) vs. effective-approximation predicted (thin dashed curves) values for the nonlinearity-induced (a) attenuation constant and (b) dephasing, for the Si-slot waveguide of Fig. 2(c). Different colors correspond to different equilibrium μ_0.

to the GHEM], we use our FEM eigenmode solver to implement a nonlinear self-consistent method (NLSCM) for the calculation of the attenuation constant and the induced dephasing in the high-power CW illumination.

The NLSCM algorithm consists of launching a given power P (in Watt) into the desired waveguide mode and iteratively re-calculating the eigenmode using the FEM solver until convergence in the eigenvalue (the complex effective index) is achieved; in each iteration, the spatial profile of graphene conductivity $\sigma^{(1)}(x,y)$ is adjusted by the locally-induced photoconductivity using the CW GHEM curves (e.g., as in Fig. 3) to map the $|\tilde{\mathbf{E}}_\parallel|(x,y)$ of the mode from the previous iteration into the $\Delta\sigma_{NL}^{(1)}(x,y)$ to be used in the following one:

$$\sigma_{j+1}^{(1)}(x,y) = \sigma_{lin}^{(1)}(x,y) + \Delta\sigma_{NL}^{(1)}\{|\tilde{\mathbf{E}}_{\parallel,j}(x,y)|\} \qquad \textbf{(18)}$$

where j is the NLSCM iteration counter. Note that the modal E-field amplitude after each iteration is re-normalized to input power P and that the *local* intensity used for look-up into the GHEM is computed by $I(x,y) = |\tilde{\mathbf{E}}_\parallel(x,y)|^2/2Z_0$. The local shift in the conductivity can be rather large for highly-confining waveguides like the Si-slot, as depicted by the final/converged spatial distribution of $\sigma^{(1)}(x)$ in Fig. 6, for a few values of $P_{NLSCM} = P$; notice how graphene's $\mathrm{Re}\{\sigma^{(1)}\}$ is practically zero over the slot region for 100 mW excitation.

The NLSCM-converged P-dependent complex effective modal index can now be converted into the complex δ_{GNL} of the NLSE Eq. (1) as

$$\delta_{GNL} = \frac{1}{2}\Delta\alpha + i\Delta\beta = ik_0\left[n_{eff,NL}(P) - n_{eff,lin}\right], \qquad \textbf{(19)}$$

where $k_0 = 2\pi/\lambda_0$. In Fig. 7 we compare the NLSCM results of Eq. (19) for the Si-slot waveguide to the effective linear approximation of Eq. (6), i.e., $\delta_{GNL} = \varsigma_{NLSE}\Delta\sigma_{NL}^{(1)}/\sigma_0$, where $\Delta\sigma_{NL}^{(1)}$ is

power-dependent as in Fig. 3 for $I_{eff} \rightarrow P/A_{eff}^G$. We find good qualitative agreement noting, however, that the effective approximation is optimistic, by a few dB in I_{sat} [panel (a)] and by 20-30% in $\Delta\beta$ for mid-range power levels [panel (b)]. Nevertheless, for the chemical potential and power levels targeted ($\mu_0 \approx 0.3$ eV and $P \approx +30$ dBm), the agreement is also quantitatively favorable. Consequently, for our NLSE/SSFM scheme, we will use the much simpler effective approximation of a constant ς_{NLSE}, which can provide valuable insight at the expense of reduced accuracy, rather than a look-up/fit to the full-wave NLSCM relation $\{\mu_0, P = |A|^2\} \rightarrow \{\Delta\alpha, \Delta\beta\}$ for each point in (z,t). Finally, we should point out that the two methods converge much better for the lower confinement waveguides, e.g., those in Fig. 2(a-b), as presented in Section 4, Fig. S1 of the Supplemental Document.

5. PULSED RESPONSE

Having completed the CW analysis, we will now present a number of pulsed applications of interest to ultrafast integrated photonics that manifest due to graphene nonlinearity in straight waveguide segments. In all the examples shown in this section, we employ the single-channel NLSE of Eq. (1), with parameters calculated for the Si-slot waveguide of Fig. 2(c) [34] for $\lambda_0 = 1550$ nm; the waveguide dispersion parameters relevant to this study are $\beta_2 = +9.84$ ps^2/m and $\beta_3 = -0.03$ ps^3/m. The GHEM presented in Section 3, coupled to the NLSE through the optical pulse power, is used to extract the photoconductivity term $\Delta\sigma_{NL}^{(1)}(z,t)$ along the propagation, which in turn nonlinearly distorts the output pulse envelope. We mainly study the effect of graphene's equilibrium chemical potential (μ_0) and the peak-power of the pulses (P_{peak}) on each application. An overview of the NLSE/GHEM algorithm implementation and the major associated quantities can be found in Section 6 of the Supplemental Document.
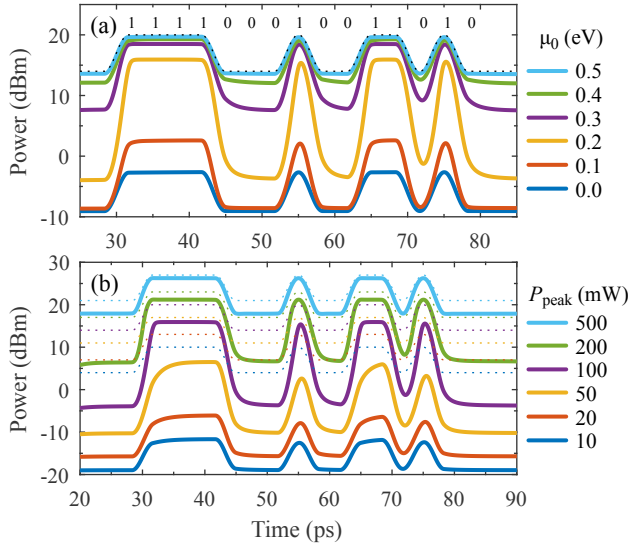
Fig. 9. Output (a) shape and (b) spectrum of a $\tau_{\text{FWHP}} = 1$ ps and $P_{\text{peak}} = 1$ W unchirped Gaussian pulse propagated along 500 μm of a graphene-overlaid Si-slot waveguide [inset in panel (a)], for three equilibrium chemical potential values. Panel (b) spectra are normalized to depict the spectral broadening.

Fig. 8. Improvement of the ER of an NRZ bitstream propagated along 100 μm of a graphene-overlaid Si-slot waveguide as a function (a) of equilibrium chemical potential for $P_{\text{peak}} = 100$ mW or (b) of peak power for $\mu_0 = 0.3$ eV. The input ER is 6 dB and the rate is 300 Gbps. Dotted curves correspond to the input pulse-streams.

A. Self-absorption modulation

The saturable absorption effect, evidenced by the GHEM for $\mu_0 < \hbar\omega/2$ in subsection C, leads to a self-absorption modulation (SAM) which can be used to passively improve the extinction ratio (ER) of an amplitude modulated signal. Low ER values can be produced by semiconductor optical amplifiers or other highly-nonlinear amplifiers. The idea behind the SA-enabled ER-improvement is that the high-power bits ('1') will experience very little losses along the waveguide (as their power is enough to saturate the $\text{Re}\{\sigma^{(1)}\}$ of graphene), while the low-power bits ('0') will experience much higher losses. As an indicative scenario, we consider a 300 Gbps NRZ-modulated stream of 16 bits with a poor extinction ratio of 6 dB, launched into a 100 μm segment of a Si-slot waveguide. The μ_0 and P_{peak} parametric results presented in Fig. 8(a) and (b), respectively, show the output pulse-streams from where we can notice that the ER improvement vs. insertion losses (IL) compromise is best for $\mu_0 \approx 0.3 \pm 0.1$ eV and for $P_{\text{peak}} \approx 50\text{-}200$ mW. Lower (or higher) values of μ_0 lead to high IL (or negligible ER improvement). P_{peak} values higher (or lower) than 100 mW suffer from low ER improvement as losses are quenched for both '1' and '0' bits (or high IL).

Finally, we note a mild distortion of the pulses due to the 300 Gbps rate leading to a rise/fall time that is comparable to intraband energy-relaxation lifetime ($\tau_\mathcal{E} = 1$ ps) but smaller than the interband recombination lifetime ($\tau_{\text{rec}} = 10$ ps). Pulse streams at rates lower than τ_{rec}^{-1} (100 Gbps) will experience much less distortion, meaning that the CW saturation curves, e.g., Fig. 3, can be used as a 'look-up' instead of the NLSE. Nevertheless, our rigorous calculation of the GHEM-induced distortion on the pulse-stream can be valuable for digital communication system analysis, i.e., extracting eye pattern metrics.
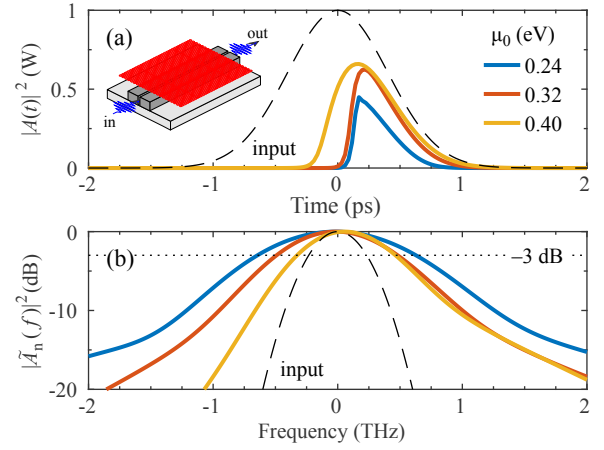
B. Pulse Shaping and Spectral Broadening

High-P_{peak} pulses benefit from reduced attenuation thanks to the deep SA which is, however, accompanied by nonlinear refraction in a form approximately analogous to the self-phase modulation (SPM) produced by the instantaneous Kerr effect in bulk nonlinear media. The SPM is equivalent to a frequency chirping, i.e., a change in the instantaneous frequency of the pulse along its duration. The combination of SPM and dispersion can give rise to interesting nonlinear phenomena like spectral broadening and soliton formation [43]. In order to probe this class of refractive nonlinear effects, we launch ps-duration pulses into a 500 μm segment of a Si-slot waveguide and study the effect of μ_0 and P_{peak}. The input pulse envelope is in all cases Gaussian shaped:

$$A(z_{\text{in}}, t) = \sqrt{P_{\text{peak}}} \exp\left[-\frac{1}{2}(1 + iC)\left(\frac{t}{\tau_0}\right)^2\right], \quad \textbf{(20)}$$

where C is the linear chirp parameter, $\tau_0 = \tau_{\text{FWHP}}/1.6651$, and τ_{FWHP} is the pulse duration (full-width half-maximum). In this subsection we use $C = 0$ (no chirping) and $\tau_{\text{FWHP}} = 1$ ps.

Figure 9 depicts the effect of μ_0 on the output pulse shape, $|A(t)|^2$, and normalized spectrum, $|\tilde{A}_{\text{n}}(f)|^2$; in this case $P_{\text{peak}} = 1$ W so that the pulse energy is approximately 1 pJ. From panel (a) we notice three interesting features as μ_0 is decreased: firstly that the pulse is more attenuated, secondly that the leading edge of the pulse becomes steeper, and, thirdly, that the temporal peaking of the pulse is slightly delayed. Moreover, from panel (b), we note that the spectrum of the pulse is broadened as μ_0 is decreased; for the $\mu_0 = 0.24$ eV case we measure a tripling of the spectral width, i.e., $B_f \approx 3$, when measured at half-power [the dotted line in panel (b)].

In order to find an optimum compromise between the IL and the B_f, we propose a figure-of-merit FOM $= B_f \times \text{IL}_{\text{lin}}$, where IL_{lin} is the power-transmission coefficient in a linear scale. We parametrically scan μ_0 and P_{peak} depicting the performance metrics in the heatmaps of Fig. 10: From panel (a) we observe that IL drops as μ_0 approaches $\hbar\omega/2 = 0.4$ eV or when the P_{peak} exceeds a threshold of 30 to 40 dBm (1 to 10 W). From panel
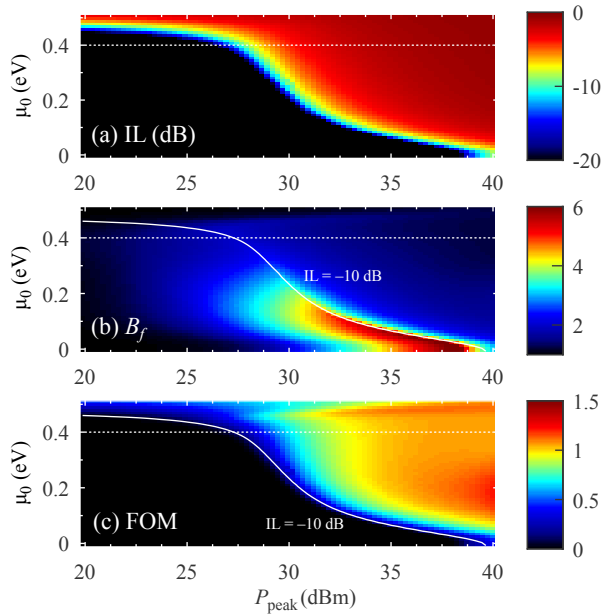
Fig. 10. Performance metrics for the pulse-shaping nonlinear functionality, as a function of pulse peak power and equilibrium chemical potential. (a) Insertion losses IL in dB, (b) spectral broadening B_f, and (c) figure-of-merit defined as $\text{FOM} = B_f \times \text{IL}_{\text{lin}}$.

(b) we observe that the B_f is largest in the above mentioned power-range and just below the $\text{IL} = -10$ dB threshold. Finally, from panel (c) we identify an interesting region between 0.4 and 0.45 eV and above 30 dBm which leads to a fair compromise of $\text{IL} > -3$ dB and $B_f \approx 2$, leading to FOM > 1.

The effect of chirping of the input pulse is parametrically investigated in Fig. S2 of the Supplemental Document, from where we note that a value of $C = -0.5$ leads to maximal B_f at $\mu_0 = 0.45$ eV. This finding is in-line with the observations in the experiment of [17] where negative chirping led to much higher spectral broadening compared to equivalent positive chirping, owing to the negative (defocusing) nonlinear refraction manifesting at $\mu_0 = 0.45$ eV, cf. Fig. 5.

C. Self Steepening and Pulse Breaking

Revisiting the 0.24 eV output pulse in Fig. 9, we note that the deep SA at the leading edge of the pulse gives rise to a self-steepening. For sufficiently higher powers and/or propagation lengths this will eventually lead to an optical shock formation [43]. In turn, the shock leads to a breaking of the pulse in time and, in combination with the nonlinear chirping, expels quasi-soliton(s) and/or dispersive waves, similar to free-carrier effects in silicon waveguides [44].

To showcase this phenomenon, we increase the pulse peak power to $P_{\text{peak}} = 8$ W and lower its duration to $\tau_{\text{FWHP}} = 125$ fs to maintain the pulse energy at approximately 1 pJ. The lowering of the pulse duration makes the waveguide length comparable to the group-velocity dispersion length, and enhances the effect. The pulse and spectrum evolution along the waveguide for a $\mu_0 = 0.2$ eV graphene sheet is depicted in Fig. 11. Notice how the shock is formed at about 100 μm and immediately a soliton-like fragment (with higher peak-power and shorter duration compared to the input pulse) is expelled; alongside that, the spectrum develops a second peak blueshifted by approximately
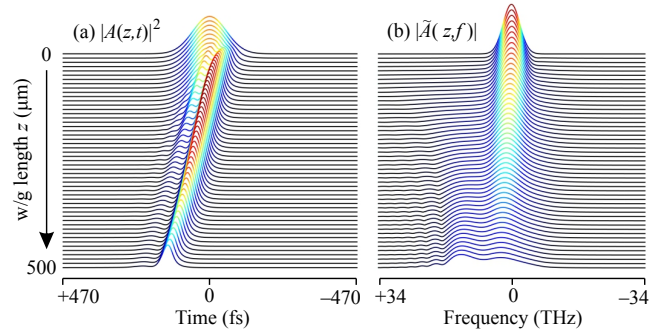

Fig. 11. Deeply sub-ps pulses experience an optical shock at the leading edge which develops into a pulse-breaking. (a) Shape and (b) spectrum of a 125 fs Gaussian pulse of 8 W peak power as it propagates along 500 μm of a 0.2 eV graphene-overlaid Si-slot waveguide.
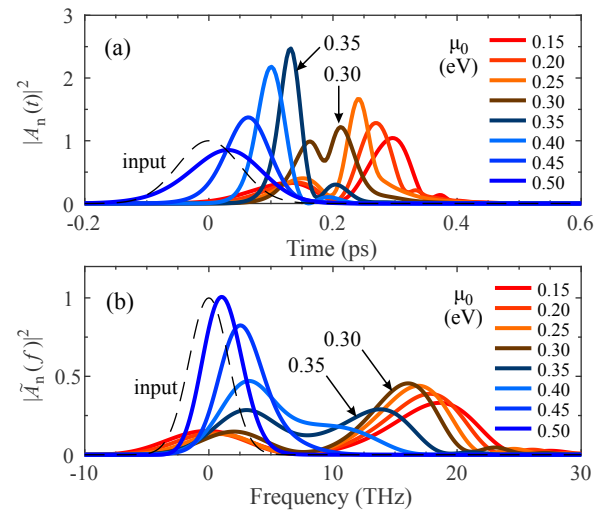

Fig. 12. Effect of equilibrium chemical potential μ_0 on pulse-breaking, for $P_{\text{peak}} = 5$ W. Both output pulse (a) shape and (b) spectrum have been normalized to the same energy level for comparison, noting that $|\mu_0| < 0.3$ eV values correspond to very high IL.

20 THz.

In order to better understand the dependence of this phenomenon on the GHEM parameters, we perform the simulation for various μ_0 values in 0.15-0.5 eV and for $P_{\text{peak}} = 5$ W. The output pulses and spectra are depicted in Fig. 12, which have all been normalized (subscript "n") to the same energy for ease of comparison; we remind that $\mu_0 < 0.3$ eV cases lead to IL higher than 20 dB for this peak-power. For instance the 0.2 eV case led to IL ≈ -6 dB in Fig. 11 ($P_{\text{peak}} = 8$ W) but IL < -30 dB here ($P_{\text{peak}} = 5$ W); this evidences the sensitivity of the output pulse shape on the input peak power, which is another signature feature of solitons. From the results in Fig. 12 we highlight the $\mu_0 = 0.3$ and 0.35 eV cases which lead to a split-pulse shape [panel (a)] and a spectral broadening factor $B_f \approx 4$ [panel (b)], respectively.

Finally, more simulation results for parametric studies of the peak-power and input chirping, at $\mu_0 = 0.35$ eV, can be found in Fig. S3 and S4 of the Supplemental Document. These further showcase the sensitivity of the quasi-solitons to these

parameters.

6. SUMMARY AND CONCLUSIONS

An electrodynamic graphene hot electron model (GHEM) was used to physically relate the optical power intensity and graphene's tunable electro-optical properties to the induced nonlinear self-acting transient photoconductivity. This model was adapted to the study of ultrafast (sub-ps) optical pulse propagation along highly-confining integrated photonic waveguides in terms of the NLSE framework. Parameters to effectively abstract the nonlinear properties of the waveguide mode for use in the NLSE were proposed and corroborated by full-wave self-consistent simulations in the static/CW regime. The NLSE-GHEM was used to simulate a number of pulsed applications (extinction-ratio improvement, pulse-shaping/spectral-broadening, and pulse-breaking leading to quasi-soliton formation) which showcase its validity and potential in a unified physically consistent modeling of both absorptive and refractive high-power nonlinearities in graphene. Our results are in good qualitative and quantitative agreement with recent experiments and can be used for the analysis and/or design of nonlinear graphene-comprising waveguide-based devices. The GHEM is also applicable to other bands besides the NIR, from the visible down to sub-THz, while the NLSE/SSFM framework can be used for any nonlinear 2D material, provided that a microscopic model (analogous to the GHEM) is used to couple the induced photoconductivity to the optical power.

Disclosures. The authors declare no conflicts of interest.

Data availability. Data underlying the results presented in this paper are not publicly available at this time but may be obtained from the authors upon reasonable request.

Supplemental document. Refer to the Supplemental Document for information pertaining to: (1) Derivation of the expression for the effective area quantifying the 2D-material/eigenmode overlap in the waveguide cross-section. (2) The governing equations for the Fermi-Dirac framework used in the graphene hot-electron model (GHEM) adopted from [32]. (3) Derivation of the singularity-free/integrable form of the interband term of graphene's surface conductivity. (4-5) Extra results that complement the core of the paper. (6) Overview summary of the NLSE/GHEM algorithm implementation and listing of the associated parameters and variables.

REFERENCES

1. N. Vermeulen, "Perspectives on nonlinear optics of graphene: Opportunities and challenges," APL Photonics **7**, 020901 (2022).
2. E. Hendry, P. J. Hale, J. Moger, A. K. Savchenko, and S. A. Mikhailov, "Coherent nonlinear optical response of graphene," Phys. Rev. Lett. **105** (2010).
3. A. H. C. Neto, F. Guinea, N. M. R. Peres, K. S. Novoselov, and A. K. Geim, "The electronic properties of graphene," Rev. Mod. Phys. **81**, 109–162 (2009).
4. F. Wang, Y. Zhang, C. Tian, C. Girit, A. Zettl, M. Crommie, and Y. R. Shen, "Gate-variable optical transitions in graphene," Science **320**, 206–209 (2008).
5. F. Bonaccorso, Z. Sun, T. Hasan, and A. C. Ferrari, "Graphene photonics and optoelectronics," Nat. Photonics **4**, 611–622 (2010).
6. M. Liu, X. Yin, and X. Zhang, "Double-layer graphene optical modulator," Nano Lett. **12**, 1482–1485 (2012).
7. S. Doukas, A. Chatzilari, A. Dagkli, A. Papagiannopoulos, and E. Lidorikis, "Deep and fast free-space electro-absorption modulation in a mobility-independent graphene-loaded Bragg resonator," Appl. Phys. Lett. **113**, 011102 (2018).
8. G. Sinatkas, T. Christopoulos, O. Tsilipakos, and E. E. Kriezis, "Comparative study of silicon photonic modulators based on transparent conducting oxide and graphene," Phys. Rev. Appl. **12** (2019).
9. L. A. Shiramin and D. V. Thourhout, "Graphene modulators and switches integrated on silicon and silicon nitride waveguide," IEEE J. Sel. Top. Quantum Electron. **23**, 94–100 (2017).
10. D. Chatzidimitriou and E. E. Kriezis, "Optical switching through graphene-induced exceptional points," J. Opt. Soc. Am. B **35**, 1525–1535 (2018).
11. M. Ono, M. Hata, M. Tsunekawa, K. Nozaki, H. Sumikura, H. Chiba, and M. Notomi, "Ultrafast and energy-efficient all-optical switching with graphene-loaded deep-subwavelength plasmonic waveguides," Nat. Photonics **14**, 37–43 (2019).
12. S. Doukas, P. Mensz, N. Myoung, A. C. Ferrari, I. Goykhman, and E. Lidorikis, "Thermionic graphene/silicon schottky infrared photodetectors," Phys. Rev. B **105** (2022).
13. I. Vangelidis, D. V. Bellas, S. Suckow, G. Dabos, S. Castilla, F. H. L. Koppens, A. C. Ferrari, N. Pleros, and E. Lidorikis, "Unbiased plasmonic-assisted integrated graphene photodetectors," ACS Photonics **9**, 1992–2007 (2022).
14. N. Vermeulen, D. Castelló-Lurbe, J. Cheng, I. Pasternak, A. Krajewska, T. Ciuk, W. Strupinski, H. Thienpont, and J. V. Erps, "Negative Kerr nonlinearity of graphene as seen via chirped-pulse-pumped self-phase modulation," Phys. Rev. Appl. **6** (2016).
15. K. Alexander, N. A. Savostianova, S. A. Mikhailov, B. Kuyken, and D. V. Thourhout, "Electrically tunable optical nonlinearities in graphene-covered SiN waveguides characterized by four-wave mixing," ACS Photonics **4**, 3039–3044 (2017).
16. K. Alexander, N. A. Savostianova, S. A. Mikhailov, D. V. Thourhout, and B. Kuyken, "Gate-tunable nonlinear refraction and absorption in graphene-covered silicon nitride waveguides," ACS Photonics **5**, 4944–4950 (2018).
17. N. Vermeulen, D. Castelló-Lurbe, M. Khoder, I. Pasternak, A. Krajewska, T. Ciuk, W. Strupinski, J. Cheng, H. Thienpont, and J. V. Erps, "Graphene's nonlinear-optical physics revealed through exponentially growing self-phase modulation," Nat. Commun. **9** (2018).
18. P. Demongodin, H. E. Dirani, J. Lhuillier, R. Crochemore, M. Kemiche, T. Wood, S. Callard, P. Rojo-Romeo, C. Sciancalepore, C. Grillet, and C. Monat, "Ultrafast saturable absorption dynamics in hybrid graphene/Si3N4 waveguides," APL Photonics **4**, 076102 (2019).
19. T. Jiang, D. Huang, J. Cheng, X. Fan, Z. Zhang, Y. Shan, Y. Yi, Y. Dai, L. Shi, K. Liu, C. Zeng, J. Zi, J. E. Sipe, Y.-R. Shen, W.-T. Liu, and S. Wu, "Gate-tunable third-order nonlinear optical response of massless Dirac fermions in graphene," Nat. Photonics **12**, 430–436 (2018).
20. G. Soavi, G. Wang, H. Rostami, A. Tomadin, O. Balci, I. Paradisanos, E. A. A. Pogna, G. Cerullo, E. Lidorikis, M. Polini, and A. C. Ferrari, "Hot electrons modulation of third-harmonic generation in graphene," ACS Photonics **6**, 2841–2849 (2019).
21. Q. Bao, H. Zhang, Y. Wang, Z. Ni, Y. Yan, Z. X. Shen, K. P. Loh, and D. Y. Tang, "Atomic-layer graphene as a saturable absorber for ultrafast pulsed lasers," Adv. Funct. Mater. **19**, 3077–3083 (2009).
22. Q. Lin, O. J. Painter, and G. P. Agrawal, "Nonlinear optical phenomena in silicon waveguides: modeling and applications," Opt. Express **15**, 16604 (2007).
23. J. L. Cheng, N. Vermeulen, and J. E. Sipe, "Third order optical nonlinearity of graphene," New J. Phys. **16**, 053014 (2014).
24. J. L. Cheng, N. Vermeulen, and J. E. Sipe, "Third-order nonlinearity of

graphene: Effects of phenomenological relaxation and finite temperature," Phys. Rev. B **91** (2015).

25. S. A. Mikhailov, "Quantum theory of the third-order nonlinear electrodynamic effects of graphene," Phys. Rev. B **93** (2016).

26. D. Chatzidimitriou, A. Pitilakis, and E. E. Kriezis, "Rigorous calculation of nonlinear parameters in graphene-comprising waveguides," J. Appl. Phys. **118**, 023105 (2015).

27. K. J. A. Ooi, L. K. Ang, and D. T. H. Tan, "Waveguide engineering of graphene's nonlinearity," Appl. Phys. Lett. **105**, 111110 (2014).

28. H. Zhang, S. Virally, Q. Bao, L. K. Ping, S. Massar, N. Godbout, and P. Kockaert, "Z-scan measurement of the nonlinear refractive index of graphene," Opt. Lett. **37**, 1856 (2012).

29. E. Dremetsika, B. Dlubak, S.-P. Gorza, C. Ciret, M.-B. Martin, S. Hofmann, P. Seneor, D. Dolfi, S. Massar, P. Emplit, and P. Kockaert, "Measuring the nonlinear refractive index of graphene using the optical Kerr effect method," Opt. Lett. **41**, 3281 (2016).

30. D. Castelló-Lurbe, H. Thienpont, and N. Vermeulen, "Predicting graphene's nonlinear-optical refractive response for propagating pulses," Laser Photonics Rev. **14**, 1900402 (2020).

31. R. Soref and B. Bennett, "Electrooptical effects in silicon," IEEE J. Quantum Electron. **23**, 123–129 (1987).

32. S. A. Mikhailov, "Theory of the strongly nonlinear electrodynamic response of graphene: A hot electron model," Phys. Rev. B **100** (2019).

33. A. Marini, J. D. Cox, and F. J. G. de Abajo, "Theory of graphene saturable absorption," Phys. Rev. B **95** (2017).

34. D. Chatzidimitriou and E. E. Kriezis, "Light propagation in nanophotonic waveguides considering graphene's saturable absorption," Phys. Rev. A **102**, 053512 (2020).

35. M. Breusing, S. Kuehn, T. Winzer, E. Malić, F. Milde, N. Severin, J. P. Rabe, C. Ropers, A. Knorr, and T. Elsaesser, "Ultrafast nonequilibrium carrier dynamics in a single graphene layer," Phys. Rev. B **83** (2011).

36. M. Baudisch, A. Marini, J. D. Cox, T. Zhu, F. Silva, S. Teichmann, M. Massicotte, F. Koppens, L. S. Levitov, F. J. G. de Abajo, and J. Biegert, "Ultrafast nonlinear optical response of Dirac fermions in graphene," Nat. Commun. **9** (2018).

37. A. Sahoo, A. Marini, and S. Roy, "Free-carrier-induced nonlinear dynamics in hybrid graphene-based photonic waveguides," Phys. Rev. A **104** (2021).

38. J. You, S. Bongu, Q. Bao, and N. Panoiu, "Nonlinear optical properties and applications of 2D materials: theoretical and experimental aspects," Nanophotonics **8**, 63–97 (2018).

39. Y. Zhang, J. Wu, Y. Yang, Y. Qu, L. Jia, T. Moein, B. Jia, and D. J. Moss, "Enhanced kerr nonlinearity and nonlinear figure of merit in silicon nanowires integrated with 2d graphene oxide films," ACS Appl. Mater. & Interfaces **12**, 33094–33103 (2020).

40. J. Wang, L. Zhang, Y. Chen, Y. Geng, X. Hong, X. Li, and Z. Cheng, "Saturable absorption in graphene-on-waveguide devices," Appl. Phys. Express **12**, 032003 (2019).

41. A. Mock, "Modeling passive mode-locking via saturable absorption in graphene using the finite-difference time-domain method," IEEE J. Quantum Electron. **53**, 1–10 (2017).

42. B. Yao, S.-W. Huang, Y. Liu, A. K. Vinod, C. Choi, M. Hoff, Y. Li, M. Yu, Z. Feng, D.-L. Kwong, Y. Huang, Y. Rao, X. Duan, and C. W. Wong, "Gate-tunable frequency combs in graphene–nitride microresonators," Nature **558**, 410–414 (2018).

43. G. Agrawal, *Nonlinear Fiber Optics*, Quantum electronics–principles and applications (Elsevier Science, 2012).

44. L. Yin, Q. Lin, and G. P. Agrawal, "Soliton fission and supercontinuum generation in silicon waveguides," Opt. Lett. **32**, 391 (2007).

45. A. Pitilakis and E. E. Kriezis, "Highly nonlinear hybrid silicon-plasmonic waveguides: analysis and optimization," J. Opt. Soc. Am. B **30**, 1954 (2013).

46. A. Pitilakis, O. Tsilipakos, and E. E. Kriezis, "Optimizing silicon-plasmonic waveguides for $\chi^{(3)}$ nonlinear applications," Appl. Phys. A **115**, 475–479 (2013).

47. A. Pitilakis, D. Chatzidimitriou, and E. E. Kriezis, "Theoretical and numerical modeling of linear and nonlinear propagation in graphene waveguides," Opt. Quantum Electron. **48** (2016).

48. A. Pitilakis, D. Chatzidimitriou, T. Yioultsis, and E. E. Kriezis, "Asymmetric si-slot coupler with nonreciprocal response based on graphene saturable absorption," IEEE J. Quantum Electron. pp. 1–1 (2021).

49. N. A. Savostianova and S. A. Mikhailov, "Optical Kerr effect in graphene: Theoretical analysis of the optical heterodyne detection technique," Phys. Rev. B **97** (2018).

50. J. B. Khurgin, "Graphene—a rather ordinary nonlinear optical material," Appl. Phys. Lett. **104**, 161116 (2014).

51. O. Tsilipakos, A. Pitilakis, A. C. Tasolamprou, T. V. Yioultsis, and E. E. Kriezis, "Computational techniques for the analysis and design of dielectric-loaded plasmonic circuitry," Opt. Quant. Electron. **42**, 541–555 (2011).

52. R. E. Glover and M. Tinkham, "Conductivity of superconducting films for photon energies between 0.3 and $40kt_c$," Phys. Rev. **108**, 243–256 (1957).

53. L. A. Falkovsky and A. A. Varlamov, "Space-time dispersion of graphene conductivity," The Eur. Phys. J. B **56**, 281–284 (2007).

Ultrafast pulse propagation in graphene-comprising nanophotonic waveguides considering non-perturbative electrodynamic nonlinearity: Supplemental Document

This documents includes supplemental information pertaining to: (1) Derivation of the expression for the effective area quantifying the 2D-material/eigenmode overlap in the waveguide cross-section. (2) The governing equations for the Fermi-Dirac framework used in the graphene hot-electron model (GHEM) adopted from [1]. (3) Derivation of the singularity-free/integrable form of the interband term of graphene's surface conductivity. (4-5) Extra results that complement the core of the paper. (6) Overview summary of the NLSE/GHEM algorithm implementation and listing of the associated parameters and variables.

1. DERIVATION OF THE GRAPHENE-WAVEGUIDE EFFECTIVE AREA

The magnitude of *local* graphene photoconductivity $\Delta\sigma_{\mathrm{NL}}^{(1)}(x,y)$ inside the waveguide cross section (xy plane) depends on the local intensity of the propagating field, $I(x,y)$ in [W/m^2], which is in turn quadratically proportional to the E-field magnitude, $|\tilde{\mathbf{E}}_\parallel(x,y)|^2$ in [(V/m)^2]; only the E-field component parallel to the 2D-material/graphene sheet interacts with it. Adopting the nomenclature of Section 2.B of the main manuscript, we can write the local field in the waveguide as

$$\mathbf{E}(x,y,z,t) = \tilde{\mathbf{e}}(\omega_0;x,y)\frac{|A(z,t)|}{\sqrt{\mathcal{P}_{\mathrm{n}}}}e^{i\beta_0 z}, \tag{S1}$$

where $\tilde{\mathbf{e}}(\omega_0;x,y)$ is the eigenmode cross section profile at operating frequency ω_0 (omitted henceforth for brevity), β_0 is the complex phase constant of the mode, $A(z,t)$ is the pulse envelope (in [W$^{1/2}$] units), and $\mathcal{P}_{\mathrm{n}}$ is a modal power-normalization constant (in [W] units). Note that Eq. (S1) applies also for the magnetic field, $\mathbf{H}(x,y,z,t)$ so that the power-flow equals $|A(z,t)|^2$.

The essence of the nonlinear Schrödinger equation (NLSE) formulation is to abstract any profile distribution in the waveguide cross-section in effective properties, characteristic of the given eigenmode. For nonlinear 2D materials, we can define an operator that calculates the effective (cross section profile averaged) value of quantity $F(x,y,z,t)$ as

$$F_{\mathrm{eff}}(z,t) = \langle F(x,y,z,t)\rangle = \frac{\int_G F(x,y,z,t)|\tilde{\mathbf{e}}_\parallel(x,y)|^2\mathrm{d}\ell}{\int_G |\tilde{\mathbf{e}}_\parallel(x,y)|^2\mathrm{d}\ell}, \tag{S2}$$

where integration takes place along the trace of graphene (or any 2D material) sheets in the cross-section and the normalization/weighting function is $|\tilde{\mathbf{e}}_\parallel(x,y)|^2$, as nonlinear quantities scale with intensity component parallel to the sheets. Applying Eq. (S2) to the full electric field $|\mathbf{E}_\parallel(x,y,t)|^2$ produces the effective value of the E-field intensity that interacts with graphene:

$$|\mathbf{E}_\parallel|_{\mathrm{eff}}^2(z,t) = \langle |\mathbf{E}_\parallel(x,y,z,t)|^2\rangle = \frac{\int_G |\mathbf{E}_\parallel(x,y,z,t)|^2|\tilde{\mathbf{e}}_\parallel(x,y)|^2\mathrm{d}\ell}{\int_G |\tilde{\mathbf{e}}_\parallel(x,y)|^2\mathrm{d}\ell}. \tag{S3}$$

Replacing the scaling of Eq. (S1) into Eq. (S3) we arrive at

$$|\mathbf{E}_\parallel|_{\mathrm{eff}}^2(z,t) = \frac{|A(z,t)|^2}{\mathcal{P}_{\mathrm{n}}}\frac{\int_G |\tilde{\mathbf{e}}_\parallel(x,y)|^4\mathrm{d}\ell}{\int_G |\tilde{\mathbf{e}}_\parallel(x,y)|^2\mathrm{d}\ell}, \tag{S4}$$

while the effective intensity on graphene (or the 2D material) is related to the effective electric field squared as

$$I_{\mathrm{eff}}(z,t) = \frac{1}{2Z_0}|\tilde{\mathbf{E}}_\parallel|_{\mathrm{eff}}^2(z,t) = \frac{|A(z,t)|^2}{A_{\mathrm{eff}}^G}. \tag{S5}$$

Finally, eliminating the (z, t)-dependent quantities between Eq. (S4) and Eq. (S5) we arrive at the effective area quantifying the cross-sectional overlap of the modal profile with graphene (or any nonlinear 2D material)

$$A_{\text{eff}}^G = \frac{2Z_0 \mathcal{P}_n}{\langle |\tilde{\mathbf{e}}_\parallel(x,y)|^2\rangle} = 2Z_0 \mathcal{P}_n \frac{\int_G |\tilde{\mathbf{e}}_\parallel(x,y)|^2 \mathrm{d}\ell}{\int_G |\tilde{\mathbf{e}}_\parallel(x,y)|^4 \mathrm{d}\ell}. \tag{S6}$$

Note that we have assumed the $I = |E_\parallel|^2/2Z_0$ relation between the intensity and E-field on the 2D material sheet, i.e., with reference to the free-space impedance Z_0. This was done for simplicity and given that a refractive index cannot be formally appointed to a zero-thickness sheet material.

2. FERMI-DIRAC FRAMEWORK

The graphene hot-electron model (GHEM) adopted from [1] relies on distinct quasi-Fermi levels (or chemical potentials) for the electron and hole plasmas, μ_e and μ_h, respectively. In general it holds that $\mu_e \neq \mu_h$, and the difference becomes more pronounced as the system is pushed farther from thermal equilibrium especially by photogeneration (interband absorption). Both plasmas have the same carrier temperature, T, which can (far) surpass the lattice temperature T_0, if even for a sub-ps timespan. In the Fermi-Dirac statistical framework, the distribution function for electrons/holes is given by

$$f_{e/h}(\mathcal{E}; \mu_{e/h}, T) = \frac{H(\pm\mathcal{E})}{1 + \exp\left(\pm\frac{\mathcal{E} - \mu_{e/h}}{k_B T}\right)}, \tag{S7}$$

where k_B is the Boltzmann constant and $H(x)$ is the step function ($H = 1$ for $x > 0$, else $H = 0$).

The solid-state parameters on which the GHEM finally relies are the carrier surface densities ($n_{e,h}$ in [$1/\text{m}^2$]) and the plasma-energy surface densities ($\mathcal{E}_{e,h}^D$ in [J/m^2]). Note that, like the distribution functions, these are distinct for electrons (e-subscript) and holes (h-subscript) and depend solely on the corresponding chemical potential ($\mu_{e,h}$) and the common carrier temperature. The formulas for the carrier and energy densities are derived from energy integrals of $f_{e/h}(\mathcal{E})$ times the density of states (DOS) which, for graphene near the tip of the Dirac cone, takes the linear form

$$N_{\text{DOS}}(\mathcal{E}) = \frac{2}{\pi(v_F \hbar)^2}|\mathcal{E}|, \tag{S8}$$

where $\hbar$ is the reduced Plank constant ($\hbar = h/2\pi$) and $v_F \approx c_0/300$ is the Fermi velocity in graphene (c_0 is the speed of light in vacuum); formally, $v_F = \alpha_0 \gamma_0 \sqrt{3}/2\hbar \approx 0.874 \times 10^6$ m/s, for a lattice constant of $a_0 = 2.46$ Å and a nearest-neighbour coupling energy of $\gamma_0 = 2.7$ eV [2, 3]. The quantities $\{n, \mathcal{E}^D\}$ are given by the following expressions: $n = \int_0^\infty N_{\text{DOS}} f \mathrm{d}\mathcal{E}$ and $\mathcal{E}^D = \int_0^\infty N_{\text{DOS}} f \mathcal{E} \mathrm{d}\mathcal{E}$, resulting in:

$$n_{e/h}(\mu_{e/h}, T) = \frac{2(k_B T)^2}{\pi(\hbar v_F)^2}F_1\left(\pm\frac{\mu_{e/h}}{k_B T}\right), \tag{S9}$$

$$\mathcal{E}_{e/h}^D(\mu_{e/h}, T) = \frac{2(k_B T)^3}{\pi(\hbar v_F)^2}F_2\left(\pm\frac{\mu_{e/h}}{k_B T}\right). \tag{S10}$$

Note the symmetry in these formulas for electrons and holes, with an attention to the sign used for electrons ($+$) and holes ($-$). The function $F_m(x)$ is the Fermi-Dirac integral (FDI) of order-m defined as

$$F_m(x) = \int_0^\infty \frac{u^m}{1 + \exp(u - x)}du. \tag{S11}$$

The total carrier and energy densities at a given state (e.g., at thermal equilibrium or quasi-equilibrium) are given by the sum of the electron and hole terms, $n_T = n_e + n_h$ and $\mathcal{E}_T^D = \mathcal{E}_e^D + \mathcal{E}_h^D$, respectively.

Finally, we stress that Eq. (S9) and Eq. (S10) are (numerically) invertible, which means that knowing any two variables in the $\{\mu, T, n\}$ or $\{\mu, T, \mathcal{E}^D\}$ set, we can calculate the third variable. In the GHEM employed in this work, we specifically require the roots of Eq. (S9) with respect to the carrier temperature T when $\mu_{e/h}$ and the corresponding $n_{e/h} = n_{e/h}^0 + n_{\text{PG}}$ are known, as well as its inversion for formulating Eqs. (12) of the main manuscript,

$$\mu_{e/h} = \pm(k_B T)F_1^{-1}\left[\frac{\pi(\hbar v_F)^2}{2(k_B T)^2}n_{e/h}\right], \tag{S12}$$

where F_1^{-1} is the inverse function of Eq. (S11) for $m = 1$. Note that asymptotic expressions can simplify the numerical inversion in extreme cases, namely $F_1(x) = x^2/2$ and $F_1(x) = e^x$, when $x \gg 1$ and $x \to 0$, respectively. Finally, fittings exist for the inverted calculation, i.e., extracting $\{\mu, T\}$ from $\{n_e, n_h\}$, such as the one proposed in [4] and its supporting information, applicable in the equilibrium case, $\mu_e \equiv \mu_h = \mu_0$.

3. GRAPHENE INTERBAND SURFACE CONDUCTIVITY

The integral in the Kubo formula for the interband contribution to the surface conductivity,

$$
\sigma_e^{(1)}(\omega, \mu_e, \mu_h, T) = \sigma_0 \frac{4i}{\pi} \int_0^\infty \frac{\hbar\omega + i\Gamma_e(\mathcal{E})}{[\hbar\omega + i\Gamma_e(\mathcal{E})]^2 - 4\mathcal{E}^2}
$$
$$
\times \left[\frac{1}{1 + \exp\left(\frac{-\mathcal{E} - \mu_h}{k_B T}\right)} - \frac{1}{1 + \exp\left(\frac{\mathcal{E} - \mu_e}{k_B T}\right)} \right] d\mathcal{E},
\tag{S13}
$$

cannot be analytically solved, even though in most practical cases the interband momentum relaxation rate is energy independent and it can even be neglected, $\Gamma_e \to 0$, under the condition $\Gamma_e \ll k_B T_0 \approx 26$ meV (at room temperature); in most practical cases $\Gamma_e < 1$ meV ($\tau_e = \hbar/\Gamma_e > 1$ ps) [5]. This complication is due to the singularity exhibited by the integrand at half-photon energy, $\mathcal{E} = \hbar\omega/2$, which can fortunately be circumvented by a transformation involving a principal value integral. This procedure has been outlined in [6] for the equilibrium case and, for the out-of-equilibrium case studied here, $\mu_e \neq \mu_h$, it can be extended as follows: We first define the auxiliary function

$$
G(\mathcal{E}; \mu_e, \mu_h, T) = \frac{\sinh\left(\frac{2\mathcal{E} - \mu_e + \mu_h}{2k_B T}\right)}{\cosh\left(\frac{\mu_h + \mu_e}{2k_B T}\right) + \cosh\left(\frac{2\mathcal{E} - \mu_e + \mu_h}{2k_B T}\right)}
\tag{S14}
$$

which can be used in compactly rewriting Eq. (S13) as

$$
\sigma_e^{(1)} = \sigma_0 \frac{4i\Omega}{\pi} \int_0^\infty \frac{G(\mathcal{E})}{\Omega^2 - 4\mathcal{E}^2} d\mathcal{E},
\tag{S15}
$$

where $\Omega = \hbar\omega + i\Gamma_e$ (the scattering rate is assumed energy independent) and the singularity at $\Omega = 2\mathcal{E}$ is evident in the denominator. Adding and subtracting the term $G(\Omega/2)$ in the nominator of the integrand in Eq. (S15), we get one singularity-free term [from the $-G(\Omega/2) + G(\mathcal{E})$ terms], that can be straightforwardly numerically computed, and one term that requires a principal-value integral (PVI) [from the $+G(\Omega/2)$ term]. Now, as the integrand function [proportional to $1/(\Omega^2 - 4\mathcal{E}^2)$] is anti-symmetric around the singularity, the PVI reduces to the proportionality constant times $i\pi$. The resulting expression for the numerically integrable interband conductivity is:

$$
\sigma_e^{(1)} = \sigma_0 \left[G(\Omega/2) + \frac{4i\Omega}{\pi} \int_0^\infty \frac{G(\mathcal{E}) - G(\Omega/2)}{\Omega^2 - 4\mathcal{E}^2} d\mathcal{E} \right].
\tag{S16}
$$

Assuming $\Gamma_e = 0$, Eq. (S16) reveals that the real and imaginary parts of the interband conductivity are solely defined by the first and second terms, respectively. Note that the real part can acquire negative values ('gain') owing to population inversion in strongly non-equilibrium states [1], i.e., when $\Delta\mu_{(e-h)} > \hbar\omega$; nevertheless, we restrict our study the cases where this regime is not entered, ensuring always that the real part of the total conductivity is positive.

4. NONLINEAR SELF-CONSISTENT METHOD

Graphene-comprising waveguides with lower mode confinement exhibit much better convergence in the nonlinearity-induced change both in attenuation coefficient and phase constant, when computed with the NLSCM (nonlinear self-consistent method) and when using the effective linear approximation $\delta_{\text{GNL}} = \varsigma_{\text{NLSE}} \Delta\sigma_{\text{NL}}^{(1)}/\sigma_0$, where $\Delta\sigma_{\text{NL}}^{(1)}$ is intensity dependent on $I_{\text{eff}} = P/A_{\text{eff}}^G$, P being the CW power launched into the waveguide mode.

Compared to the highly-confining Si-slot waveguide presented in Fig. 7 of Section 4.B of the main manuscript, the SNOI (silicon nitride on insulator) waveguides from [7, 8] show almost identical results when employing both approaches [NLSCM or linear effective approximation of Eq. (6)], Fig. S1. However, note also that a much higher power (+10 dB or more) is required to saturate the losses and that the induced nonlinear refraction $\Delta\beta$ is lower (5 times).
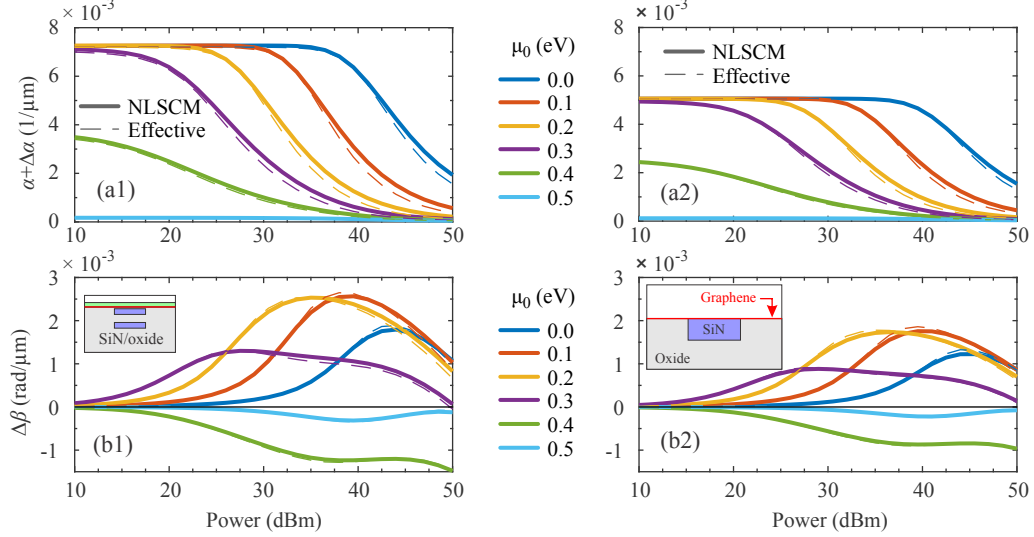
Fig. S1. Comparison between the NLSCM-calculated vs. effective-approximation predicted values for the nonlinearity-induced (a1-a2) attenuation constant and (b1-b2) dephasing, for the vertical SNOI slot waveguide [7] (left panels) and for the buried SiN ridge waveguide [8] (right panels).

5. PULSED RESPONSE

A. Pulse Shaping and Spectral Broadening

We parametrically vary the chirp of the input pulses, for a few equilibrium chemical potential values near the $\mu_0 = 0.45$ eV point identified in the main manuscript, Fig. 10(c). In Fig. S2 we can see that chirping of the input pulse has an important effect on the spectral broadening factor B_f, which is also reflected on the FOM, with a value of $C = -0.5$ being the best option.
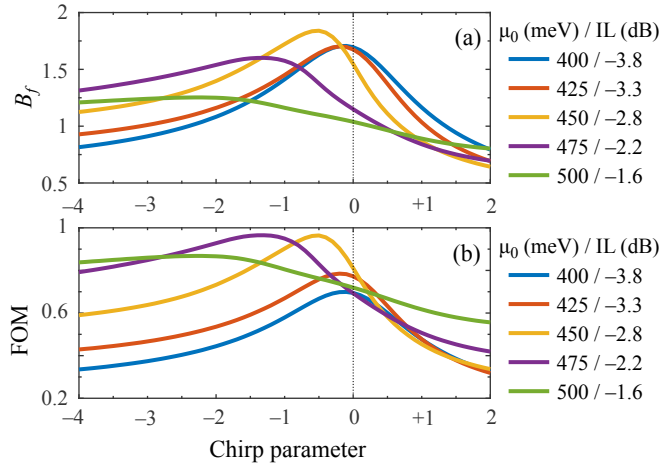

Fig. S2. Chirping of the input Gaussian pulse can significantly affect (a) the spectral broadening factor B_f and (b) the overall FOM $= B_f \times \text{IL}_{\text{lin}}$. The insertion losses (IL) only depend on the equilibrium chemical potential value, given in the legend in dB units. Pulse peak power is 1 W, full-width half-power is 1 ps, and Si-slot waveguide length is 0.5 mm.

B. Self Steepening and Pulse Breaking

The effect of peak-power and chirping of the input 125 fs pulse are parameterically studied here using the NLSE-GHEM. The Si-slot waveguide length is 0.5 mm (500 μm) and is covered by a graphene monolayer with an equilibrium chemical potential of $\mu_0 = 0.35$ eV.

4

In Fig. S3 we note how only a narrow input peak-power value range, e.g., close to $P_{\text{peak}} = 5$ W, produces a pronounced quasi-soliton feature (higher peak and shorter duration) in the output pulse. Lower or higher power values lead to similar but less pronounced features.
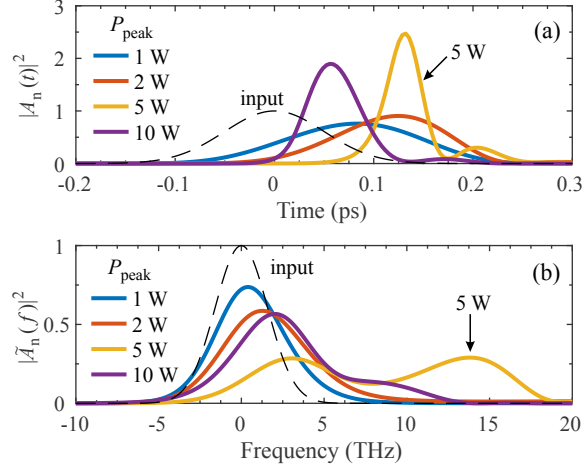

Fig. S3. Effect of pulse peak-power P_{peak} on pulse-breaking, for $\mu_0 = 0.35$ eV. Both pulse (a) shape and (b) spectrum have been normalized to the same energy level for comparison, noting that $P_{\text{peak}} < 5$ W values correspond to very high IL.

From Fig. S4 we can infer that changes in the input pulse chirp can displace the peak of the output-pulse spectrum by almost 10 THz.
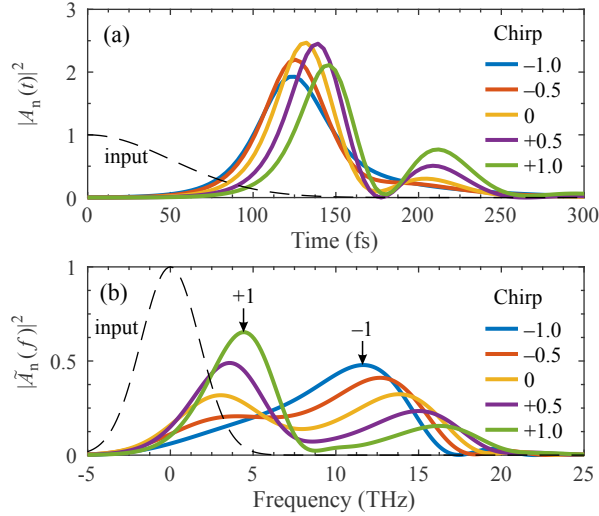

Fig. S4. Effect of chirping on pulse-breaking, for $P_{\text{peak}} = 5$ W and $\mu_0 = 0.35$ eV. Both pulse (a) shape and (b) spectrum have been normalized to the same energy for comparison.

6. OVERVIEW OF THE NLSE/GHEM ALGORITHM IMPLEMENTATION

In order to replicate the results presented in this paper the following three modules are needed:
- Firstly, a waveguide mode solver to extract the modal constants/coefficients of the NLSE. This is typically used only once for each waveguide type and operating wavelength. Iterative usage of the mode solver is required only for the nonlinear self-consistent method (NLSCM), used here to validate the simplified model adopted. Our mode solver is based on the finite-element method and was custom-built in MATLAB [9].

Symbol	Units	Description	Calculated with...
$A(t)$	$W^{0.5}$	Complex optical pulse envelope (retarded-time)	User-defined
n_{eff}	.	Complex effective mode index ($n_{\text{eff}} = \beta_0/k_0$)	Mode solver
α	$1/m$	Linear modal power-attenuation	Mode solver
β_m	s^m/m	Dispersion coefficient ($m \geq 2$)	Mode solver
γ_{NL}	$1/m/W$	Complex third-order/Kerr nonlinear coefficient	Mode solver
ς_{NLSE}	$1/m$	Photoconductivity scaling factor	Mode solver
A_{eff}^G	m^2	Effective area for mode-graphene overlap	Mode solver
μ_0	J (or eV)	Equilibrium chemical potential of graphene	User-defined
$\tau_{\mathcal{E}}$	s	Intraband energy relaxation lifetime	User-defined
τ_{rec}	s	Carrier recombination lifetime	User-defined
$\Gamma_i(\mathcal{E})$	J (or eV)	Graphene intraband momentum scattering rate	User-defined
$\mu_{e/h}(t)$	J (or eV)	Transient chemical potentials for electrons/holes	GHEM
$\mu_{e_0/h_0}(t)$	J (or eV)	Transient quasi-equilibrium chemical potentials	GHEM
$n_{\text{PG}}(t)$	$1/m^2$	Transient photo-generated carrier density	GHEM
$\mathcal{E}_T^D(t)$	J/m^2	Transient total plasma energy density	GHEM
$T(t)$	K	Transient hot-carrier temperature	Fermi-Dirac
$n_{e/h}(t)$	$1/m^2$	Transient carrier densities	Fermi-Dirac
$\sigma_{i/e}^{(1)}(t)$	S	Transient intra/interband conductivity (complex)	Kubo formulas
$\Delta\sigma_{\text{NL}}^{(1)}(t)$	S	Transient graphene photoconductivity (complex)	Kubo formulas

Table S1. Summary of the major parameters and coefficients underlying the NLSE/GHEM method developed in this work. The symbols, units, and brief description/usage is also given.

- Secondly, an implementation of the transient solution to the GHEM equation system, i.e., a 'time-integrator'. In essence, for a given optical pulse this calculates the transient photoconductivity, which is a nonlinear/time-domain term in the NLSE. We used MATLAB to solve the equation system in the transient/pulsed and static regime[1]. This work focuses mostly on the transient solution, to study the dynamics of the system, but the static response was also needed to extract the maps that helped to identify the optimal graphene-sheet configurations (e.g. Fig. 5 of the main manuscript).

- Thirdly, an implementation of the SSFM algorithm to solve the NLSE, i.e., a 'step-propagator' that slides the input pulse envelope along the nonlinear waveguide and thus calculates the output (nonlinearity-distorted) pulse envelope. This algorithm in described near the end of subsection 2.2 of the main manuscript, with six steps. Note that the 'time-integrator' described in the previous module is used (once) in each step of the SSFM. We implemented the SSFM in MATLAB, making use of PARFOR for efficient parametric sweeps.

The major parameters and variables appearing in this work, and their usage and means of calculation, are listed in Table S1. The GHEM equation system and Kubo formulas are given in Section 3.1 and 3.2 of the main manuscript, respectively. The Fermi-Dirac formulas are given in Section 2 of this document.

---

[1]The GHEM involves multiple differential *and* algebraic equations (DAEs), so it forms a relatively stiff ODE system with a singular mass matrix. In the transient regime, we solved it using MATLAB's ODE15S which is a variable-step, variable-order (VSVO) solver based on the numerical differentiation formulas (NDFs) of orders 1 to 5. In the static regime, we used standard root-finding algorithms implemented in MATLAB's FSOLVE (e.g. trust-region Powell's "dog leg" method); normalization of the equations and educated starting guesses are recommended to ease the numerical algorithm convergence.

REFERENCES

1. S. A. Mikhailov, "Theory of the strongly nonlinear electrodynamic response of graphene: A hot electron model," Phys. Rev. B **100** (2019).
2. J. L. Cheng, N. Vermeulen, and J. E. Sipe, "Third order optical nonlinearity of graphene," New J. Phys. **16**, 053014 (2014).
3. A. H. C. Neto, F. Guinea, N. M. R. Peres, K. S. Novoselov, and A. K. Geim, "The electronic properties of graphene," Rev. Mod. Phys. **81**, 109–162 (2009).
4. D. Castelló-Lurbe, H. Thienpont, and N. Vermeulen, "Predicting graphene's nonlinear-optical refractive response for propagating pulses," Laser Photonics Rev. **14**, 1900402 (2020).
5. T. Gu, N. Petrone, J. F. McMillan, A. van der Zande, M. Yu, G. Q. Lo, D. L. Kwong, J. Hone, and C. W. Wong, "Regenerative oscillation and four-wave mixing in graphene optoelectronics," Nat. Photonics **6**, 554–559 (2012).
6. L. A. Falkovsky, "Optical properties of doped graphene layers," J. Exp. Theor. Phys. **106**, 575–580 (2008).
7. N. Vermeulen, D. Castelló-Lurbe, M. Khoder, I. Pasternak, A. Krajewska, T. Ciuk, W. Strupinski, J. Cheng, H. Thienpont, and J. V. Erps, "Graphene's nonlinear-optical physics revealed through exponentially growing self-phase modulation," Nat. Commun. **9** (2018).
8. P. Demongodin, H. E. Dirani, J. Lhuillier, R. Crochemore, M. Kemiche, T. Wood, S. Callard, P. Rojo-Romeo, C. Sciancalepore, C. Grillet, and C. Monat, "Ultrafast saturable absorption dynamics in hybrid graphene/Si3N4 waveguides," APL Photonics **4**, 076102 (2019).
9. O. Tsilipakos, A. Pitilakis, A. C. Tasolamprou, T. V. Yioultsis, and E. E. Kriezis, "Computational techniques for the analysis and design of dielectric-loaded plasmonic circuitry," Opt. Quant. Electron. **42**, 541–555 (2011).